

AD-A128 124

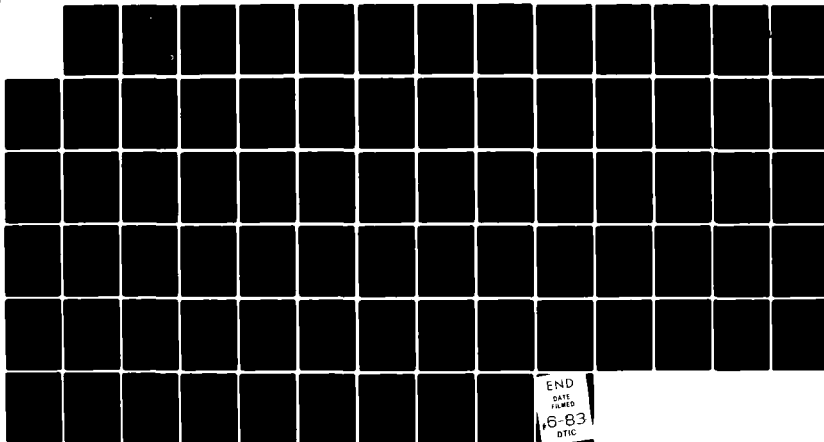
IMPULSE RESPONSE OF THE OCEAN FLOOR: MATHEMATICAL  
MODELING(U) NAVAL AIR DEVELOPMENT CENTER WARMINSTER PA  
SENSORS AND AVIONICS TECHNOLOGY DIRECTORATE  
T B GABRIELSON APR 83 NADC-82254-30

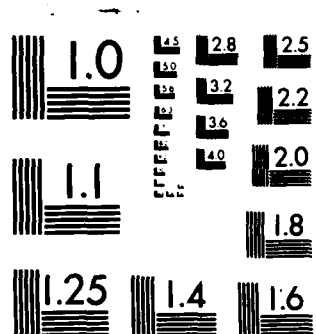
1/1

UNCLASSIFIED

F/G 20/1

NL





MICROCOPY RESOLUTION TEST CHART  
NATIONAL BUREAU OF STANDARDS-1963-A

AD A 128124

(12)

REPORT NO. NADC-82254-30



IMPULSE RESPONSE OF THE OCEAN FLOOR:  
MATHEMATICAL MODELING

Thomas B. Gabrielson  
Sensors Avionics Technology Directorate  
NAVAL AIR DEVELOPMENT CENTER  
Warminster, Pennsylvania 18974

April 1983

Final Report  
Task No. ZR01108

APPROVED FOR PUBLIC RELEASE; DISTRIBUTION UNLIMITED

Prepared for  
NAVAL AIR DEVELOPMENT CENTER  
Warminster, Pennsylvania 18974

DTIC  
ELECTE  
MAY 16 1983

DTIC FILE COPY

83 05 16 061

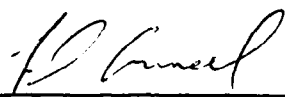
## NOTICES

**REPORT NUMBERING SYSTEM** — The numbering of technical project reports issued by the Naval Air Development Center is arranged for specific identification purposes. Each number consists of the Center acronym, the calendar year in which the number was assigned, the sequence number of the report within the specific calendar year, and the official 2-digit correspondence code of the Command Office or the Functional Directorate responsible for the report. For example: Report No. NADC-78015-20 indicates the fifteenth Center report for the year 1978, and prepared by the Systems Directorate. The numerical codes are as follows:

CODE	OFFICE OR DIRECTORATE
00	Commander, Naval Air Development Center
01	Technical Director, Naval Air Development Center
02	Comptroller
10	Directorate Command Projects
20	Systems Directorate
30	Sensors & Avionics Technology Directorate
40	Communication & Navigation Technology Directorate
50	Software Computer Directorate
60	Aircraft & Crew Systems Technology Directorate
70	Planning Assessment Resources
80	Engineering Support Group

**PRODUCT ENDORSEMENT** — The discussion or instructions concerning commercial products herein do not constitute an endorsement by the Government nor do they convey or imply the license or right to use such products.

APPROVED BY: \_\_\_\_\_

  
FREDERICK D. AMEEL  
DEPUTY DIRECTOR, SATD

DATE: \_\_\_\_\_

26 Apr 83

UNCLASSIFIED

SECURITY CLASSIFICATION OF THIS PAGE (When Data Entered)

REPORT DOCUMENTATION PAGE		READ INSTRUCTIONS BEFORE COMPLETING FORM
1. REPORT NUMBER NADC-82254-30	2. GOVT ACCESSION NO. AD-A128124	3. RECIPIENT'S CATALOG NUMBER
4. TITLE (and Subtitle)  Impulse Response of the Ocean Floor: Mathematical Modeling		5. TYPE OF REPORT & PERIOD COVERED  FINAL
		6. PERFORMING ORG. REPORT NUMBER
7. AUTHOR(s)  Thomas B. Gabrielson		8. CONTRACT OR GRANT NUMBER(s)  NAVAIR DEV CEN INDEPENDENT RESEARCH FUNDS
9. PERFORMING ORGANIZATION NAME AND ADDRESS  Sensors and Avionics Technology Directorate Naval Air Development Center Warminster, PA 18974		10. PROGRAM ELEMENT, PROJECT, TASK AREA & WORK UNIT NUMBERS  Task No. ZR01108
11. CONTROLLING OFFICE NAME AND ADDRESS  Naval Air Development Center Warminster, PA 18974		12. REPORT DATE April 1983
14. MONITORING AGENCY NAME & ADDRESS (if different from Controlling Office)		13. NUMBER OF PAGES 68
		15. SECURITY CLASS. (of this report)  UNCLASSIFIED
		15a. DECLASSIFICATION/DOWNGRADING SCHEDULE
16. DISTRIBUTION STATEMENT (of this Report)  Approved for Public Release; Distribution Unlimited		
17. DISTRIBUTION STATEMENT (of the abstract entered in Block 20, if different from Report)		
18. SUPPLEMENTARY NOTES		
19. KEY WORDS (Continue on reverse side if necessary and identify by block number)  Ocean Floor Acoustics Ocean Floor Measurements Impulse Response Mathematical Modeling		
20. ABSTRACT (Continue on reverse side if necessary and identify by block number)  Success in probing the ocean floor acoustically depends on the ability to resolve physical features. Since this amounts to temporal resolution of the received signal, short-duration transient signals are ideal for these measurements. Procedures for propagation prediction of such acoustic transients are developed as a tool for interpreting ocean floor measurements. Some of the special features of time-dependent propagation are discussed in contrast with the usual continuous wave solutions and asymptotic solutions for the field integral are related to various types of propagation.		

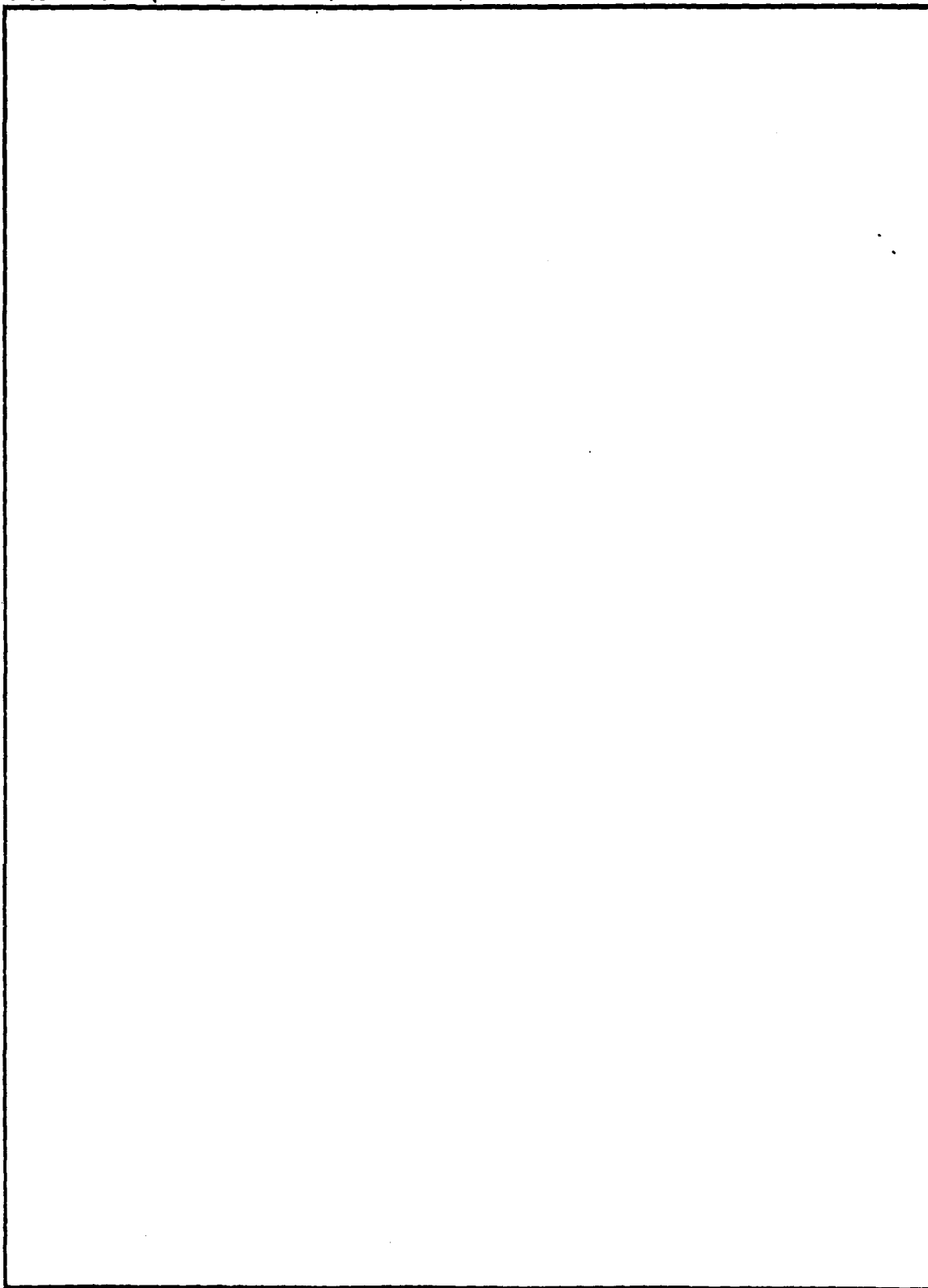
DD FORM 1 JAN 73 1473

EDITION OF 1 NOV 68 IS OBSOLETE

UNCLASSIFIED

SECURITY CLASSIFICATION OF THIS PAGE (When Data Entered)

SECURITY CLASSIFICATION OF THIS PAGE (When Data Entered)



SECURITY CLASSIFICATION OF THIS PAGE (When Data Entered)

# LIST OF FIGURES

Figure		Page
1	Generalized physical model of ocean floor . . . . .	4
2	Single, constant sound speed layer over solid basement . . . . .	10
3	Single gradient layer over solid basement . . . . .	11
4	Ray/plane-wave composite model for transient propagation . . . . .	15
5	Geometry for reflection and displacement of ray from a point source . . . . .	18
6	Geometric construction for ray spreading loss including field displacement . . . . .	24
7	Homogeneous fluid layer over a perfectly rigid reflector. . . . .	26
8	Two possible branch cuts in the $\gamma$ -plane . . . . .	28
9	Locator diagram for stationary phase points . . . . .	30
10	Steepest descent path and saddle points for reflection coefficient and exponential factor of equation (27) . . . . .	31
11	Steepest descent path and saddle points for entire integrand of equation (27) . . . . .	32
12	Migration of saddle points and descent contour associated with pole E for increasing range: (a) $r = 200m$ , (b) $r = 300m$ , (c) $r = 400m$ . . . . .	33
13	Comparison of ray/plane-wave solution(—) with spherical wave solution (....) near critical angle reflection from fluid half-space . . . . .	43
14	Predicted time series for reflection from pitch by spherical wave theory . . . . .	47
15	Predicted time series for reflection from plaster-of-paris. . . . .	49
16	Predicted time series for reflection from iron . . . . .	50
A-1	Generalized model of the ocean floor as a layered reflector . . . . .	A-2
B-1	Correct digit comparison for Airy series . . . . .	B-9
B-2	Origin-shifted series analysis . . . . .	B-10
B-3	Division of complex Z-plane for numerical computation of Airy functions . . . . .	B-11



Accession For	
NTIS GRA&I	<input checked="" type="checkbox"/>
DTIC TAB	<input type="checkbox"/>
Unannounced	<input type="checkbox"/>
Justification	
Distribution/	
Availability Codes	
Avail and/or Special	

## CONTENTS

	Page
List of Figures . . . . .	ii
Summary . . . . .	1
Introduction . . . . .	1
The Physical Model . . . . .	3
Plane Wave Solution . . . . .	5
Spherical Wave Solution . . . . .	14
Reflection From a Thin Layer . . . . .	25
Numerical Implementation . . . . .	36
Applications . . . . .	41
Conclusions . . . . .	51
References . . . . .	53
Appendix A - Reflection From a Multilayered Medium . . . . .	A-1
Appendix B - Airy Functions . . . . .	B-1



## SUMMARY

This report summarizes the second phase of research in nonlinear signal enhancement of underwater acoustic measurements. The first phase,<sup>1</sup> in which the nonlinear process was developed and digitally implemented, generated the need for a mathematical model of the reflection of transient acoustic signals from the ocean floor. This model is necessary both for verifying the signal enhancement process by predicting the ideal response of a typical ocean floor and for interpreting measurements that have been enhanced. Of course, many continuous wave models are available for prediction purposes but, in this work, a model was needed that could predict a time-varying field and relate the time-domain features to specific propagation mechanisms.

Several classes of transient-response models have been developed and tested ranging from a simple ray model to a numerical integration of the complete field integral. The simple model assumes that reflection at the ocean floor can be described by the plane wave reflection coefficient and the remainder of the path spreading and direction can be determined by ray tracing (geometrical acoustics). While this model is only valid for high frequency or deep water, it is flexible and inexpensive to run. Multiple propagation paths are easily handled as are arbitrary source waveforms.

At the other extreme is the integration of the field integral and, while this procedure can be expensive, all of the wave effects (interface waves, diffraction) are properly accounted for. For low frequency (below 100 Hz), shallow water (several wavelengths or less) or source/receiver near the ocean floor, these wave effects can be critical. Several examples of application of this model to actual measurements are given in which the various wave effects can be seen.

Of intermediate complexity and cost is an asymptotic model based on approximate solution of the full wave integral. This solution accounts for multiple paths in the ocean floor, trapped propagation through the ocean floor, and field displacement on reflection. As an added feature, the asymptotic solution breaks up into a number of terms each of which corresponds to a physical mode of propagation in the bottom.

While these models were designed and developed primarily as an aid in the interpretation of ocean floor seismic measurements, they will be valuable in any circumstance involving propagation of transients.

## INTRODUCTION

Modern systems for acoustic detection and localization of submarines and surface ships must function in a wide range of environments. Detection may be desired at very long ranges if large ocean areas must be protected or at shorter ranges if the guard areas are straits or passages. Again, depending on the area, detection and localization may have to be done in deep or shallow water, over rough or smooth regions of the ocean floor and in many different conditions of water temperature structure. Depending on the specific target and tactics, the detection or localization system may operate across a

wide spread of frequencies and the sensor itself (the hydrophone or hydrophone array) may be anywhere in the water column from near the surface to on the bottom.

In some of these operating environments, the ocean floor plays only a minor role in the transmission of acoustic energy from source to sensor but there are three cases in which the ocean floor can greatly influence propagation:

- a. low acoustic frequency - below about 100 Hz in typical ocean situations,
- b. shallow water - acoustic wavelength is of the order of water depth, and
- c. near-bottom sensors - sensor is within an order of the wavelength of the bottom.

For sensor environments other than these three, the ocean floor can often be adequately treated as a planar, lossy reflector. To do so in the above-mentioned situations will, however, introduce serious errors into the predicted behavior of the bottom.

Since accurate prediction of acoustic propagation is crucial not only to design and evaluation of new sensors but also to design of tactics, knowledge of the acoustical behavior of the ocean floor is a vital part of sonar sensor research and application. Unfortunately, the ocean floor has still not been well characterized at low frequency. Thousands of measurements of ocean bottom properties have been made by many laboratories but most of these measurements are either not applicable to system operation below 100 Hz or have not been analyzed for this information in particular. The NAVAIRDEVCECEN itself has hundreds of seismic measurements from sites around the world<sup>2</sup> and these are only recently being enhanced<sup>1</sup> sufficiently to be useful for detailed bottom property estimation.

Because the ocean floor is often responsible for several distinct paths of propagation, short-duration pulses are ideal for making the necessary property measurements. A sharply pulsed source results in separate received pulses corresponding to each path from source to receiver. Transient signals are, however, considerably more difficult to model theoretically than continuous wave (CW) signals and this theoretical modeling is necessary in order to interpret measurements physically.

Assumption of continuous, sinusoidal excitation causes the wave equation to degenerate into a simpler differential equation that can be solved by (for example) normal modes in a straightforward manner. If, on the other hand, the excitation is transient then either the wave equation must be solved directly or the CW solution must be integrated over frequency. In this report, we will not consider direct solution of the wave equation but rather we will develop several solution techniques based on integration of the CW solution. While CW solutions are common and highly developed, transient or time-dependent solutions are not, so the models developed as a part of this work will be generally useful as an adjunct to acoustic studies of the ocean floor.

## THE PHYSICAL MODEL

Before we actually construct a model for the acoustical behavior of the ocean floor, let us consider the relevant acoustic properties. The most important property, sound speed, is the speed at which a small disturbance travels through the medium. Changes in sound speed within the medium cause refraction or bending of the sound waves (primary effect) and diffraction of the field (secondary effect) into regions not reached by geometrical rays. Discontinuities in sound speed occurring at boundaries between media of different types cause reflection (primary effect) and formation of interface waves (secondary effect).

In fluids, acoustic waves are compressional waves which are characterized by a compressional sound speed that is a function of both the density and the compressibility of the fluid. Thus, we will also need to know the density (or the compressibility) of the fluid in order to describe its behavior for no-loss propagation.

Elastic solids, on the other hand, support two distinct types of waves: compressional and shear waves. We then have another sound speed based on the density and resistance to shear or twisting deformation of the solid and another set of waves that can be reflected or refracted and can form interface waves. We will also consider dissipation or attenuation of shear and compressional waves in order to represent the real ocean floor materials more accurately.

Certain simplifications will need to be made in our representation of these properties so that the resulting model is not prohibitively complicated. For example, we will not consider boundary roughness or slope. Since our principal interest is in low frequency propagation, this will not be too restrictive an assumption. In addition, we will restrict variations in sound speed to one dimension (depth) and further restrict the sound speed to be either piece-wise constant or of an analytical form that allows solution in terms of special functions.

One final assumption concerns the manner in which attenuation is modeled. Particularly in fluid-saturated sediments, the mechanisms for energy dissipation can be complicated. The usual viscous resistance of the fluid is combined with the friction between sediment grains and, possibly, the interaction of entrained gases. Data are sparse on these processes and, even if measurements were available, incorporation of such a complicated process into a computer program would be a major undertaking. Consequently, we will approximate any attenuation process as a viscous damping process in which the dissipation per cycle is constant. This is only valid over limited ranges of frequency.

Figure 1 illustrates the physical model that will be used for most of this research. This model consists of a solid basement half-space over which lies a fluid layer with variable properties. This fluid layer can either have constant sound speed in which case the field variables will vary as linear combinations of sines and cosines or  $1/c^2$  linear in depth in which case the solutions will be linear combinations of Airy functions. Since many models are available for acoustic propagation in water, we will not consider this part of the problem; hence, we will use a homogeneous half-space of fluid above our ocean floor model.

## GEOFYSICAL MODEL

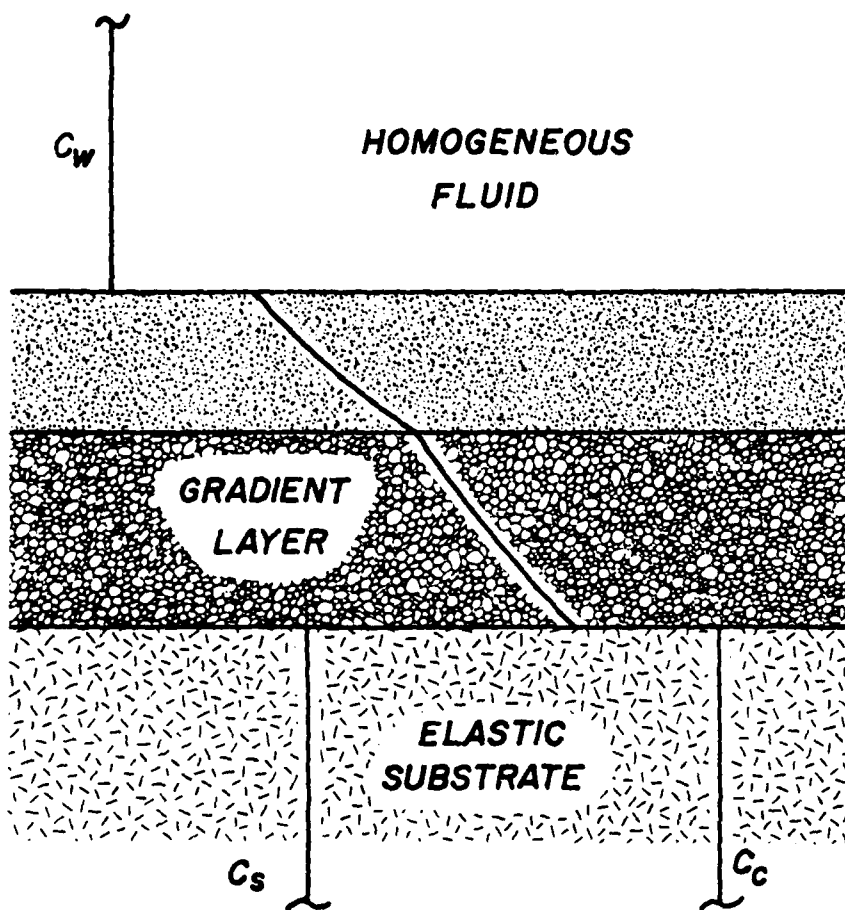


Figure 1. Generalized physical model of ocean floor.

While this is a very simple model, it does allow most of the important types of acoustic propagation to be represented. Furthermore, addition of layers is straightforward and would permit more accurate modeling of sound speed profiles in sediments.

In the following two sections, we will discuss the two major theoretical approaches toward calculation of the reflected field from this bottom model. The simpler procedure involves assuming that the incident energy is in the form of plane waves. The plane wave reflection coefficient is relatively easy to compute, and a fairly complicated field can be approximated by adding different plane wave solutions together. Unfortunately, a number of interesting and sometimes significant effects are not treated. Interface waves, for example, are not excited according to plane wave theory.

The second type of solution procedure takes into account the curvature of the waves emanating from a point source. This method is quite time-consuming but it does provide an exact solution and will be useful in establishing the extent of the effects omitted by the plane wave solution.

#### PLANE WAVE SOLUTION

Although it exists in three-dimensional space, a plane wave is essentially one-dimensional. Its wavefront is a plane and the medium is displaced by its passage only in the direction perpendicular to this plane. A true plane wave can only remain plane in a medium of constant sound speed; however, we will consider waves that are approximately plane (or, locally plane) so that we can apply this theory to our inhomogeneous ocean floor model.

True plane waves are solutions of the three-dimensional wave equation for constant sound speed,

$$\frac{\partial^2 \phi}{\partial x^2} + \frac{\partial^2 \phi}{\partial y^2} + \frac{\partial^2 \phi}{\partial z^2} = \frac{1}{c^2} \frac{\partial^2 \phi}{\partial t^2} \quad (1)$$

where

$c$  = sound speed

$\phi$  = some scalar property of the field (pressure, velocity potential).

If we assume harmonic functions of the form  $e^{-i\omega t}$  and separate the field quantity  $\phi$  into a range-dependent factor and a depth-dependent factor, we can write three ordinary differential equations: two for the range function and one for the depth function. The depth function equation is,

$$\frac{d^2 U}{dz^2} + [k^2(z) - \gamma^2] U = 0 \quad (2)$$

where

$$k = \omega/c(z)$$

$U$  = depth function of field property

$\gamma$  = horizontal wave number

If the sound speed is constant, the solutions of equation (2) are,

$$U = e^{\pm i\beta z}$$

where

$\beta$  = vertical wave number

$$= \sqrt{k^2 - \gamma^2} \text{ so that } k^2 = \gamma^2 + \beta^2.$$

In conjunction with the harmonic factor  $e^{-i\omega t}$ , these solutions represent waves with a vertical component of motion: the positive sign corresponds to movement in the  $+z$  direction and the negative sign to movement in the  $-z$  direction. This is true in general for the  $e^{-i\omega t}$  dependence. If the coefficient of a wave number component is positive then the wavefront is moving in the positive direction along the corresponding axis. Keep this feature in mind when we discuss the equations for reflection. This distinction between positive and negative-going waves will allow separation of the incident and reflected fields.

The complete solution to equation (1) is,

$$\phi = \phi_0 e^{i[\vec{k} \cdot \vec{R} - \omega t]} \quad (3)$$

where

$\vec{k}$  = vector wave number,  $\gamma_x \vec{i} + \gamma_y \vec{j} + \beta \vec{k}$

$\vec{R}$  = position vector,  $x\vec{i} + y\vec{j} + z\vec{k}$

$\omega$  = angular frequency,  $2\pi f$

$\phi_0$  = amplitude

and

$$\gamma_x^2 + \gamma_y^2 + \beta^2 = k^2 = (\omega/c)^2.$$

The vector wave number gives the direction of the normal to the wavefront and  $\omega$  gives the frequency of oscillation for the single frequency wave or equation (3).

Since the properties of a plane wave are identical anywhere on a plane perpendicular to the wave number vector (i.e., on a wavefront), boundary conditions are very simple to write. For a fluid-fluid boundary, we must maintain continuity of displacement (or velocity) normal to the boundary and continuity of pressure across the boundary. At a fluid-solid boundary, the condition of zero resistance to transverse displacement of the solid is also needed.

Only the lower half-space of our physical model is elastic so we will not consider propagation in elastic media; just reflection from them. The plane wave reflection coefficient is the ratio of reflected field amplitude to incident field amplitude. For a fluid over an elastic half-space, the plane wave reflection coefficient is,<sup>3</sup>

$$V = \frac{G_1 - G}{G_1 + G} \quad (4)$$

where

$$G = \rho_1 B_2 / \rho_2$$

$$G_1 = B_1 ((2f-1)^2 + 4f^2 B_2 B_s)$$

$$B_{1,2} = \sqrt{(c_v^2 / c_{1,2}^2) - 1}$$

$$B_s = \sqrt{(c_v^2 / \beta^2)}$$

$\beta$  = shear sound speed of solid

$c_1$  = compressional sound speed of fluid

$c_2$  = compressional sound speed of solid

$c_v$  = vertex velocity of wave ( $v = \omega / c_v$ )

$$f = \beta^2 / c_v^2$$

$\rho_1$  = density of fluid

$\rho_2$  = density of solid

Because we will be placing a layer over the solid, we will need to use this reflection coefficient as a boundary condition.<sup>4</sup> First, we write the pressure in a homogeneous fluid overlying the solid half-space (the z-axis being perpendicular to the interface),

$$p = p_0 [e^{-iz} + V e^{iz}]$$

where

$p_0$  = pressure amplitude of incident wave

$z$  = vertical wave number

and the normal derivative of the pressure (which is proportional to particle velocity),

$$\frac{\partial p}{\partial z} = i\beta p_0 \left[ -e^{-i\beta z} + Ve^{i\beta z} \right]$$

The ratio of these quantities is proportional to acoustic impedance and can be used as a boundary condition. At the interface,  $z=0$ ; therefore this impedance is,

$$\xi_0 \equiv \frac{p}{\partial p / \partial z} \bigg|_{z=0} = \frac{i(1+V)}{\beta(1-V)} \quad (5)$$

This relation will be identical for any quantity that is a solution of the wave equation.

At this point, we must also consider the addition of attenuation to this model. We will assume viscous attenuation which is a constant loss per cycle equivalent to the addition of imaginary part (linear in frequency) to the wave number,

$$k' = k + i\omega\alpha \quad (6)$$

so that the plane wave function becomes,

$$e^{ik'R} = e^{-\omega\alpha R} e^{ikR}$$

and the loss  $A$  (in decibels) over some distance  $\Delta r$  is,

$$\begin{aligned} A &= -20 \log [e^{-\omega\alpha\Delta r}] \\ &= 8.69 \omega\alpha\Delta r \end{aligned}$$

This loss is generally given in decibels per distance  $\Delta r$  at some frequency  $f$ , therefore,

$$\alpha = \frac{A}{54.6 f \Delta r} \quad (7)$$

In practice, the attenuation is inserted by modifying the sound speed, not the wave number. Equation (6) can be written,

$$k' = \omega/c' = \omega[1 + i\alpha c]/c$$

therefore,

$$c' = c/(1 + i\alpha c) \quad (8)$$

This substitution will allow the ad hoc addition of small amounts of attenuation to relations derived for conservative systems like the reflection coefficient equation (4).



Next, let us consider reflection of plane waves from a fluid layer over a solid basement. Appendix A presents a solution for the general case of a multilayered reflector, so we can just simplify these results. For a constant sound speed layer, the model is shown in Figure 2. In the fluid half-space, the field can be written as,

$$\phi_0 = e^{-i\beta_0 z} + V_t e^{i\beta_0 z}$$

where

$V_t$  = plane wave reflection coefficient of layer plus basement

$\phi_0$  = velocity potential.

Also, the field in the layer is,

$$\phi_1 = a_1 \cos \beta_1 z + b_1 \sin \beta_1 z.$$

Using equation (A-4), we can evaluate the ratio of coefficients of  $\phi_1$ ,

$$r_1 = \frac{\sin \beta_1 h + \xi \cos \beta_1 h}{\cos \beta_1 h - \xi \sin \beta_1 h} \quad (9)$$

where  $\xi$  is given by equations (4) and (5). The overall reflection coefficient is then given by equations (A-2) and (A-3),

$$V_t = \frac{1}{r_0} = \frac{\beta_1 + i r_1 \beta_0 \rho_1 / \rho_0}{-\beta_1 + i r_1 \beta_0 \rho_1 / \rho_0} \quad (10)$$

We will also consider a layer with variable sound speed: in particular,

$$1/c^2(z) = 1/c_1^2 - g_1 z \quad (11)$$

This model is shown in figure 3 and the solutions associated with this sound speed function are discussed in appendix B. The resulting field expression is a linear combination of these solutions (called Airy functions),

$$\phi_1 = a_1 A_i(Z_1) + b_1 B_i(Z_1) \quad (12)$$

where

$A_i, B_i$  = Airy functions

and, from equation (B-5),

$$Z_1 = qz - \frac{1}{q^2} \left( \frac{z^2}{c_1^2} - \frac{1}{2} \right) \quad (13)$$

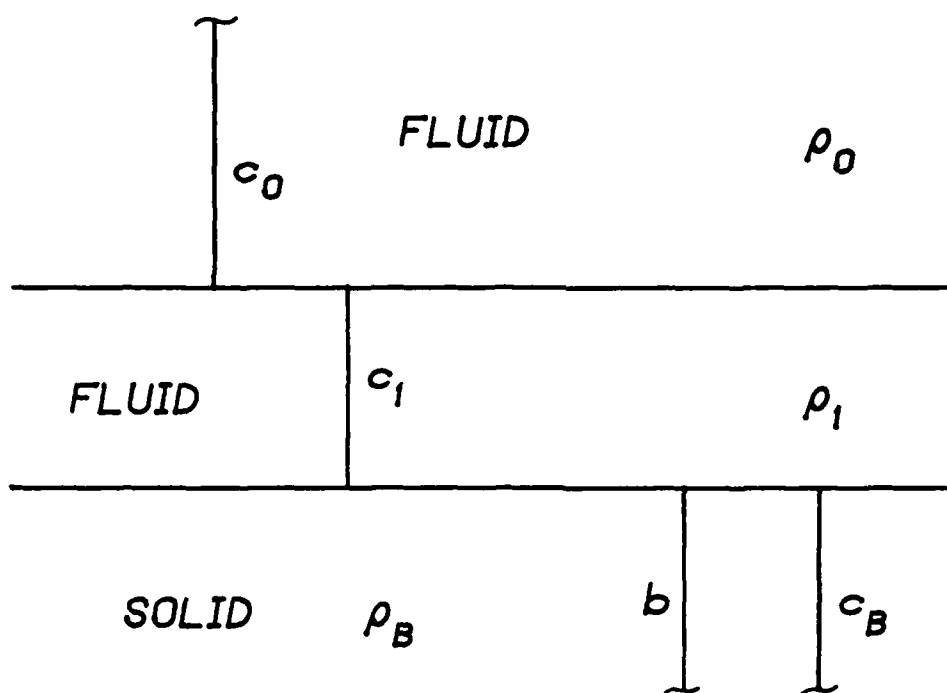


Figure 2. Single, constant sound speed layer over solid basement.

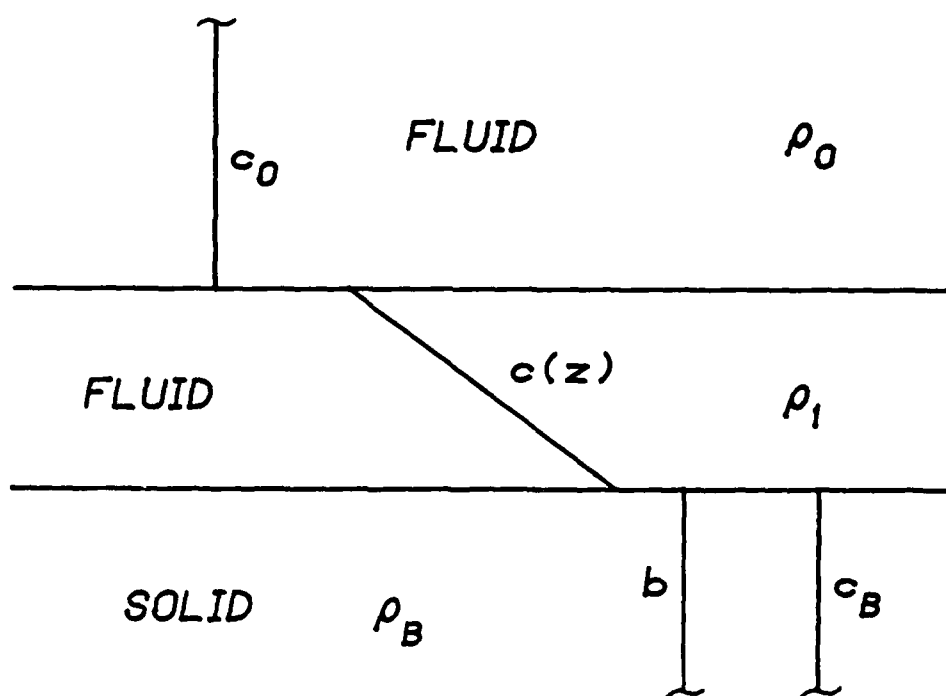


Figure 3. Single gradient layer over solid basement.

where

$$q = (g_1 \omega^2)^{1/3}.$$

Therefore,

$$\frac{\partial A_i}{\partial z} = \frac{\partial A_i}{\partial Z} \frac{\partial Z}{\partial z} = q A_i' (Z). \quad (14)$$

As in the case of the constant sound speed layer, we solve for the overall reflection coefficient by means of equations (A-4), (A-3), and (A-2) of appendix A. These yield, respectively,

$$r_1 = \frac{-B_i(Z_1) + q \xi B_i'(Z_1)}{A_i(Z_1) - q \xi A_i'(Z_1)} \bigg|_{z=-h} \quad (15)$$

$$r_0 = \frac{-\rho_0 [r_1 A_i' + B_i'] + i \beta_0 \rho_1 [r_1 A_i + B_i]}{\rho_0 [r_1 A_i' + B_i'] + i \beta_0 \rho_1 [r_1 A_i + B_i]} \quad (16)$$

and

$$V_t = 1/r_0.$$

We now are able to compute the reflection coefficient for either a constant sound speed layer over a solid (equations (5), (9), and (10)) or a gradient layer over a solid (equations (5), (15), and (16)). Each of these equation sets provides a value for  $V_t$  for a specific frequency and a specific incident angle of the wavefront. This incident angle is actually determined by the components of the wave number vector so that we will use  $\gamma$ , the horizontal wave number as the independent variable. The relationships between  $\gamma$ ,  $\beta$ , and the grazing angle  $\theta$  (angle to the horizontal plane) of the wavefront normal are,

$$\begin{aligned} \gamma &= k \cos \theta \\ \beta &= k \sin \theta \\ k^2 &= \gamma^2 + \beta^2. \end{aligned} \quad (17)$$

Although these single-layer models are very simple, they do include most of the important types of propagation. The gradient layer model allows reflection from the top of the layer, refraction within the layer, reflection from the solid basement, and interface propagation along both the fluid-fluid and the fluid-solid interfaces.

As we have mentioned, one calculation of  $V_t$  is needed for each frequency and each grazing angle. In order to compute the response of this model to an impulse, we must first compute the reflection coefficient at many frequencies throughout the band of interest. The inverse Fourier transform then yields the impulse response in the time domain. For a specific incidence angle (which we would normally compute for a particular path by ray tracing through the ocean medium), the time-domain response is as follows,

$$p(t) = \frac{1}{2\pi} \int_{-\infty}^{\infty} V_t(\omega) e^{-i\omega t} d\omega \quad (18)$$

where

$p$  = acoustic pressure.

(The  $-i\omega t$  exponent reflects our choice of  $e^{-i\omega t}$  as the harmonic time dependence of the acoustic disturbance. This is contrary to the convention in signal processing.) While we have derived  $V_t$  in terms of the velocity potential  $\phi$ , we can consider it to be the pressure reflection coefficient also since both  $p$  and  $\phi$  identically satisfy the wave equation. Equation (18) gives the pressure time-history for the reflection of a unit pressure impulse. This result is identical to the velocity potential time-history for an incident unit impulse of velocity potential. A source of unit pressure impulse is considerably easier to understand than a unit impulse of velocity potential so we will continue our discussion in terms of pressure only.

Once we have found the impulse response, we can add a source waveform in one of two ways. In the time domain, the source time function can be convolved with the impulse response to produce the time history for reflection of that source waveform,

$$r(t) = p(t) * s(t) \quad (19)$$

where

$p(t)$  = impulse response of reflector by equation (18)

$r(t)$  = reflected signal

$s(t)$  = source waveform.

Alternatively, we can make use of the fact that a convolution in the time domain is a multiplication in the frequency domain and multiply the reflection coefficient  $V_t$  by the source spectrum prior to transforming so that,

$$r(t) = \frac{1}{2\pi} \int_{-\infty}^{\infty} V_t(\omega) S(\omega) e^{-i\omega t} d\omega \quad (20)$$

where

$S(\omega)$  = Fourier transform of  $s(t)$

$$= \int_{-\infty}^{\infty} s(t)e^{i\omega t} dt.$$

In short, the procedure for computing the time-domain response for a particular propagation path given a nonsinusoidal source is as follows: compute the water path from source to ocean floor to receiver by ray tracing. Using the grazing angle (relative to the ocean floor at the point of reflection) of this ray, calculate the horizontal wave number and then compute  $V_t$  at many frequencies across the band of interest. Adjust this result for the spreading, time delay, and phase shifting incurred along the ray path in the water. Multiply this function by the spectrum of the source waveshape and take the inverse Fourier transform. The result is then the received signal for the selected propagation path. Plane wave reflection theory is used to account for the effects of the reflection model (the layer and solid basement, in this case) while ray theory is used to predict the water-borne effects. We can repeat this procedure for as many paths as are significant in a particular environment and combine the results, as shown in figure 4, to produce a complete prediction for the received signal.

This technique for building a signal from its component parts is a flexible and computationally fast method for predicting the propagation of transient acoustic energy. It is, however, limited by the restrictions of both ray theory and plane wave reflection theory. In instances in which the source or receiver is near the ocean floor, or in shallow water, or at low frequency, this approach may be inadequate. In these circumstances, interface waves, both compressional and shear, may contribute substantially to the field. There may also be considerable diffraction at low frequency which cannot be predicted by ray tracing methods. For these reasons, we will consider in the next section a more sophisticated and, consequently, a more expensive model that represents the wave field itself without the approximations implicit in ray tracing and plane wave reflection.

#### SPHERICAL WAVE SOLUTION

A small source (small in relation to the dimensions of the medium and boundaries) generates a spherical wavefront in a homogeneous medium and such a wave acts differently at boundary reflection than a plane wave. Usually, the assumption is made that the source is far enough removed from any boundaries so that the wavefront may be considered plane. As we will see, this assumption cannot be justified at low frequency or when the source is near the ocean bottom. We will develop a quantitative measure by which we can determine the validity of the plane wave assumption in any practical case but for now it is sufficient to recognize that in some instances wavefront curvature cannot be neglected.

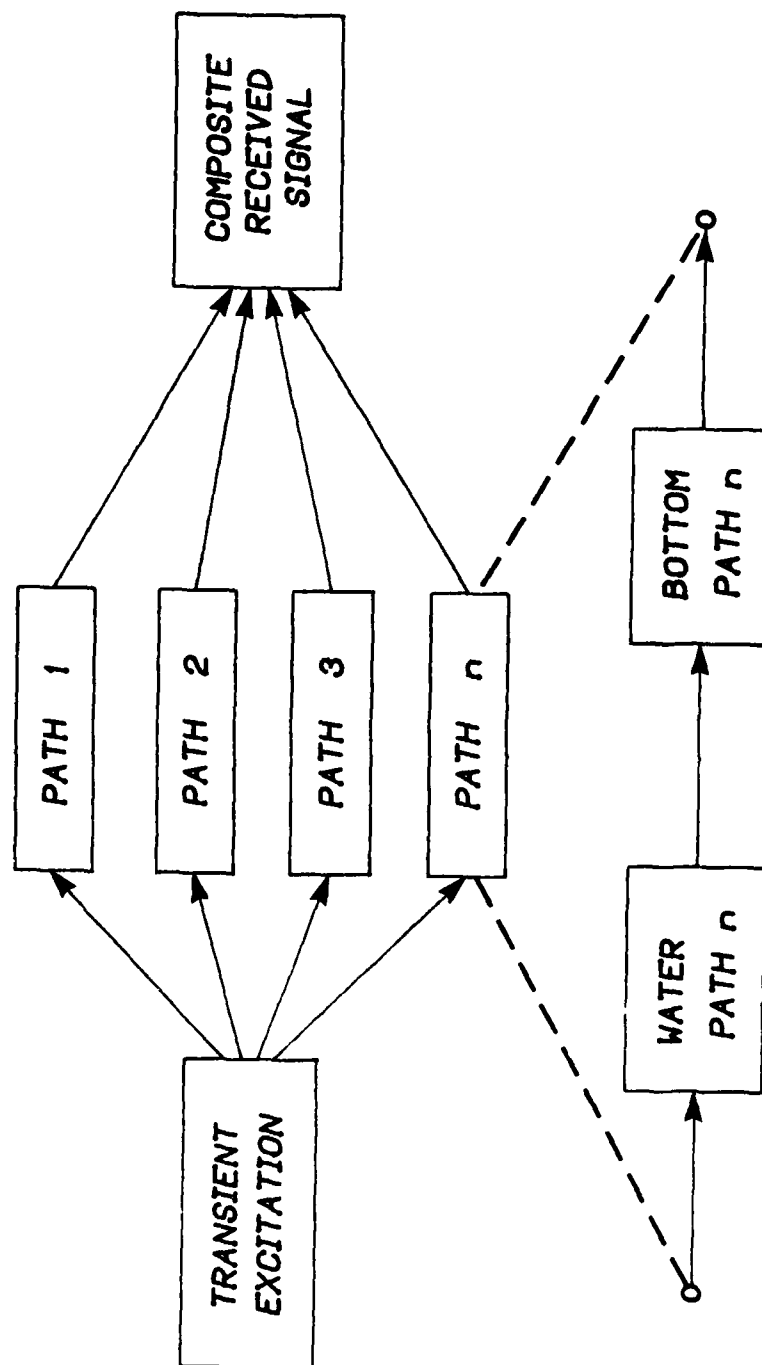


Figure 4. Ray/plane-wave composite model for transient propagation.

In a homogeneous fluid, the free-field expression for a harmonic point source is,

$$\phi = \frac{e^{i(kR-\omega t)}}{R} \quad (21)$$

where

$k$  = wave number,  $\omega/c$

$R$  = distance from source

$\phi$  = velocity potential.

This is the simplest expression of a spherical wave and it is true not only for velocity potential but for any field quantity (pressure, particle velocity, displacement potential) that satisfies the Helmholtz equation for acoustic vibrations. Also, the expression is true in the immediate vicinity of a point source in an inhomogeneous medium.

Unfortunately, equation (21) is spherically symmetric while the boundaries are typically parallel planes. Therefore, either cylindrical or Cartesian coordinates would be more suitable for ocean propagation problems. Just as the spherical wave, given by equation (21), is the elementary solution of the vibration equation in spherical coordinates, the plane wave, equation (3), is the elementary solution in Cartesian coordinates and the cylindrical wave,

$$\phi = J_0(\gamma r) e^{i(\pm \beta z - \omega t)} \quad (22)$$

is the elementary solution in cylindrical coordinates.

Since an integral superposition over wave number of the elementary plane wave solutions is a Fourier transform integral and the result must be identical to the free-field expression, equation (21), we can invert the transform to find the weighting function.<sup>5</sup> The complete superposition integral can then be written,

$$\frac{e^{i(kR-\omega t)}}{R} = \frac{i e^{-i\omega t}}{2\pi} \iint_{-\infty}^{\infty} \frac{e^{i\vec{k} \cdot \vec{R}}}{\beta} d\gamma_x d\gamma_y \quad (23)$$

where

$\gamma_x, \gamma_y$  = x, y components of horizontal wave number  $\gamma$ .

Notice that the integral comprises the elementary plane wave expression  $e^{i\vec{k} \cdot \vec{R}}$  and a weighting function  $i/(2\pi\beta)$ .



Furthermore, an integral superposition of the elementary cylindrical waves is a Hankel transform and can be inverted similarly. The result is identical to a conversion of equation (23) to cylindrical coordinates,

$$\frac{e^{i(kR-\omega t)}}{R} = i e^{-i\omega t} \int_0^{\infty} \frac{J_0(\gamma r) e^{i\beta z}}{\beta} \gamma d\gamma \quad (24)$$

Figure 5 illustrates the general reflection geometry that we will consider. In particular, a point source and receiver are located above an inhomogeneous half-space that is characterized by a plane wave reflection coefficient. Since equations (23) and (24) were derived for the source located at  $z=0$ , we will have to modify the expressions accordingly.

Actually, two field expressions are required: one for the propagation directly from the source to the receiver ( $r$  units horizontally and  $d-z$  units vertically); and one for the propagation from the source down to the half-space, modification by the reflection coefficient, and up to the receiver ( $r$  units horizontally and a total of  $d+z$  units vertically). Only this second field is of interest here. In terms of plane waves, this field is,

$$\phi = \frac{ie^{-i\omega t}}{2\pi} \iint_{-\infty}^{\infty} \frac{e^{i(\gamma_x x + \gamma_y y)} e^{i\beta(z+d)}}{\beta} V(\gamma) d\gamma_x d\gamma_y$$

or, in cylindrical coordinates,

$$\phi = ie^{-i\omega t} \int_0^{\infty} \frac{J_0(\gamma r) e^{i\beta(z+d)}}{\beta} V(\gamma) \gamma d\gamma. \quad (25)$$

This integral can be interpreted as follows: first, the point source is represented as an infinite sum of plane waves each travelling in the direction given by the horizontal wave number  $\gamma$ . The horizontal wave number is related to the constant wave number by the angle of the direction of propagation with the horizontal,

$$\gamma = k \cos \theta.$$

Hence, as  $\gamma$  increases, the plane wave travels more nearly horizontal. Eventually,  $\gamma$  is greater than  $k$  and this angle becomes imaginary. These waves are evanescent waves. They travel horizontally but the field amplitude decays exponentially in the vertical direction. This can be seen by substituting an imaginary  $\beta$  into the elementary plane wave expression, equation (3). The vertical wave number,

$$\beta = k \sin \theta = \sqrt{k^2 - \gamma^2}$$

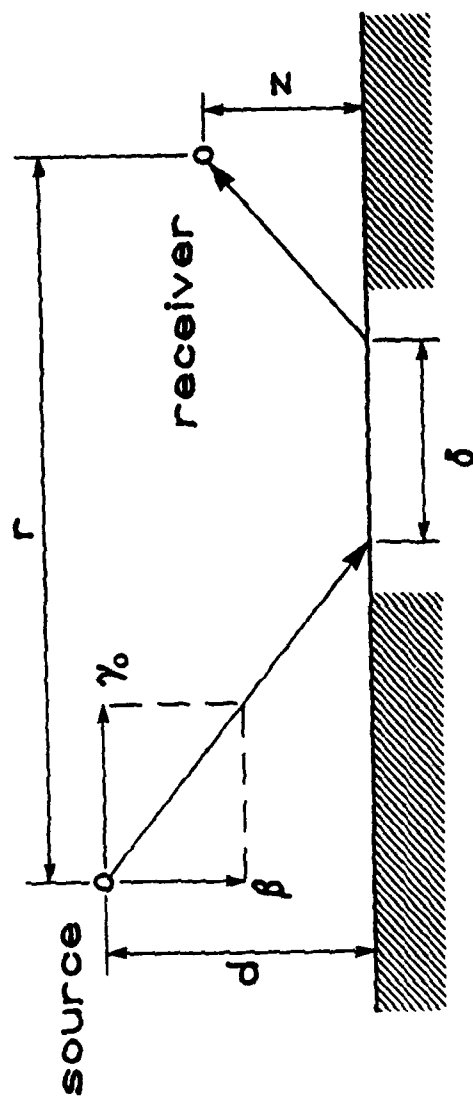


Figure 5. Geometry for reflection and displacement of ray from a point source.

becomes imaginary when  $\gamma$  is greater than  $k$ . The integral of equation (25) thus states that a point source cannot be completely described by superposition of real plane wave but these evanescent waves must be included also.

The second point to notice in equation (25) is that the elementary waves inside the integral are each modified by the appropriate value of the plane wave reflection coefficient. In this way, the influence of the inhomogeneous reflector is accounted for completely. Finally, the exponent involving the vertical wave number is positive which correctly describes the upward direction of travel of the reflected field.

Equation (25) then describes the field at the receiver point including all of the effects of the reflecting medium. Unlike the plane wave model, this expression explicitly involves the source and receiver locations so that the solutions will not be as simple to extend to other geometries as they were with the plane wave model. We do, however, have a means for describing all of the types of propagation that result from the reflecting medium. Before we solve this equation numerically, we will examine some of the properties of this equation through an approximate analytical technique.

By using the identities,<sup>6</sup>

$$J_0(\gamma r) = \frac{1}{2} \left[ H_0^{(1)}(\gamma r) + H_0^{(2)}(\gamma r) \right]$$

$$H_0^{(1)}(\gamma r) = -H_0^{(2)}(-\gamma r)$$

where

$$H_0^{(1)}, H_0^{(2)} = \text{Hankel functions,}$$

we can rewrite equation (25) in the following form,

$$\phi = \frac{i e^{-i\omega t}}{2} \int_{-\infty}^{\infty} H_0^{(1)}(\gamma r) \frac{e^{i\beta(z+d)}}{\beta} V(\gamma) \gamma d\gamma \quad (26)$$

as long as  $V(\gamma) = V(-\gamma)$ . This, of course, is always true for physically realizable problems since it does not matter whether the plane wave is coming from the right or the left - only the magnitude of the angle is important.

If  $\gamma r$  is large compared to 1, we can further reduce the integral by using the asymptotic form of  $H_0^{(1)}$ ,

$$H_0^{(1)}(\gamma r) \approx \sqrt{\frac{2}{\pi \gamma r}} e^{i(\gamma r - \pi/4)}.$$

Equation (26) becomes,

$$\phi = \frac{i e^{-i(\omega t + \pi/4)}}{\sqrt{2\pi r}} \int_{-\infty}^{\infty} \frac{e^{i[\gamma r + \beta(z+d)]}}{\beta} V(\gamma) \sqrt{\gamma} d\gamma \quad (27)$$

This is the form of the integral that we will consider in the following approximate techniques. Although we will not consider this aspect until the next section, notice that the integral itself has the form of a Fourier transform,

$$I = \int_{-\infty}^{\infty} F(\gamma) e^{i\gamma r} d\gamma \quad (28)$$

where

$$F(\gamma) = \frac{V(\gamma) \sqrt{\gamma}}{\beta} e^{i\beta(z+d)}$$

As a result, the solution can be computed by means of the fast Fourier transform (FFT) algorithm.

We can learn quite a bit about the physics of reflection by considering the integral in equation (27) as a complex contour integral. In general, the reflection coefficient  $V$  will have poles for some complex (and possibly, some real) values of  $\gamma$  and a nontrivial branch cut emanating from the value of  $\gamma$  at which  $\beta=0$ . As we will see, each of these singularities is related to a specific type of propagation and it is possible to isolate these mechanisms in the solution process.

Given that equation (27) is a complex contour integral, there are several ways to find a solution. First, the integral can be evaluated (numerically) along the original contour which is the real axis of the  $\gamma$ -plane. Second, the contour can be deformed in such a way that only pole residues and branch line integrals remain and the branch line integrals can be evaluated numerically. Also, the contour can be deformed so that it passes through the saddle points of the integrand. The contribution to the integral's value becomes concentrated at these saddle points and the integral can be evaluated approximately in the neighborhood of each saddle and the remainder of the path can be neglected. Finally, various combinations of these methods may be used as long as the rules for contour deformation are observed.

The direct integration method and the residue/branch-line-integral solution are standard methods so we will only consider them briefly in subsequent discussions. The steepest descent method or saddle point method is based on locating the regions in the  $\gamma$ -plane in which the integral becomes concentrated and then determining the integral's value in these regions.<sup>3,7</sup> Since the integral is concentrated in a small area, the value can be found by series approximation. In addition, the regions of concentration (the saddle points) correspond to physical propagation mechanisms.

To locate the saddle points, we first separate the integrand into a slowly varying magnitude function and a complex exponential. In our case, the reflection coefficient phase can vary quite rapidly so we will have to consider this phase as part of the complex exponential. Thus, we can write the integral part of equation (27) as,

$$I = \int_{-\infty}^{\infty} \frac{V_m(\gamma)\sqrt{\gamma}}{\beta} e^{i[\gamma r + \beta(z+d) + \dots]} d\gamma \quad (29)$$

where

$$V(\gamma) = V_m(\gamma)e^{i\phi(\gamma)}$$

and we will assume that the factor  $V_m\sqrt{\gamma}/\beta$  is slowly varying. This is not, in fact, true in some instances (particularly near  $\beta=0$ ) but as long as we are aware of the assumption we will be able to compensate for any problems it introduces.

Since the exponent of the exponential in equation (29) is, in general, complex, it controls the rate of change not only of the phase of the integrand but also of the magnitude (as long as the rest of the integrand is slowly varying). We would expect that if the phase is changing rapidly, the individual elements of the integration will add out of phase and, therefore, contribute little to the integral's value. On the other hand, when the phase of the integrand is stationary, the elements will add constructively. At the saddle point, both the magnitude and phase are stationary and we can find a path through this point along which the magnitude decay is most rapid. This is the path of steepest descent and, by virtue of the behavior of analytic functions, the phase along this path is constant. Physically, this means that the integral is actually made of discrete groups of wavefront arrivals. Each group is given by a small amount of waves of slightly different wave number that are in-phase at the receiver point. The saddle points locate each of these groups.

In order to locate the saddle points and descent paths, rewrite equation (29) in the following form,

$$I = \int_{-\infty}^{\infty} G(\gamma)e^{f(\gamma)} d\gamma \quad (30)$$

where

$$\begin{aligned} f(\gamma) &= i[\gamma r + \beta(z+d) + \dots]/kR \\ G(\gamma) &= V_m\sqrt{\gamma}/\beta \\ R &= \sqrt{r^2 + (z+d)^2} \\ &= kR. \end{aligned}$$

The parameter  $\rho$  is introduced so that we have an adjustment on the rate of descent of the function away from the saddle point. When  $\rho$  is large, the magnitude will decrease quickly on either side of the saddle and our approximation will be good. The stationary points of the exponent are given by,

$$\frac{\partial f}{\partial \gamma} = 0$$

or

$$\frac{i}{kR} \left[ r + \frac{\partial \phi}{\partial \gamma} - \frac{\gamma}{\beta} (z + d) \right] = 0$$

or

$$r - \frac{\gamma_0}{\beta} (z + d) = - \left. \frac{\partial \phi}{\partial \gamma} \right|_{\gamma_0} \quad (31)$$

At this point, let us examine the geometry of the reflection process. In figure 5, we have shown the ray path (the normal to the wavefront) for a wave with horizontal wave number  $\gamma_0$ . The length of the projection of the legs of the ray path onto the interface is  $\gamma_0(z + d)/\beta$ . Thus, the displacement of the field on reflection is given by the difference,

$$r - \frac{\gamma_0}{\beta} (z + d) = \delta$$

which is, by equation (31),

$$\delta = - \left. \frac{\partial \phi}{\partial \gamma} \right|_{\gamma_0} \quad (32)$$

This quantity is usually known as beam displacement because of its derivation in terms of bounded beams<sup>3</sup>, but any nonplanar wavefront exhibits a similar displacement so field displacement may be a more appropriate term.

Notice that, if we had not included the phase of the reflection coefficient in the exponent, we would have obtained the naive result that there is no displacement of the field on reflection. The most obvious case in which there is a displacement of the field is a reflector that is a positive gradient half-space. A ray that enters the gradient half-space will eventually exit further downrange as it is refracted upwards by the sound speed gradient. The displacement given by equation (32) is identical to the displacement given by ray theory. There is also a displacement on reflection from a homogeneous half-space. This is a wave phenomenon as ray theory predicts no such displacement. This displacement has, however, been observed experimentally.<sup>3</sup>

By the method of steepest descent the integral's value resulting from one saddle point is,

$$I_0 \approx e^{\rho f(\gamma_0)} \sqrt{\frac{-2\pi}{\rho f''(\gamma_0)}} G(\gamma_0) \quad (33)$$

where only the first term of the series expansion of  $G$  about the saddle point has been retained. As long as  $kR \gg 1$ , this will be a valid approximation. Substituting equation (33) for the integral in equation (27), we can write the field as,

$$\psi = V(\gamma_0) e^{i[\gamma_0 r + \beta(z+d) - \omega t]} \sqrt{\frac{\gamma}{r\beta^2 \frac{\partial}{\partial \gamma} [\frac{\gamma}{\beta}(z+d) + \delta]}} \quad (34)$$

The significance of the factor under the radical is not immediately obvious but it represents the geometrical spreading loss over the propagation path including the displacement on reflection. This can be seen in the construction shown in figure 6.

The geometrical spreading loss is given by the square root of the ratio of the elemental areas  $\epsilon_m$  and  $\epsilon_0 m_0$ :

$$\sqrt{\frac{\epsilon_0 m_0}{\epsilon_m}} = \frac{\psi}{\psi_0} = \sqrt{\frac{r}{r\beta^2 \frac{\partial}{\partial \gamma} [\frac{\gamma}{\beta}(z+d) + \delta]}}$$

(The field intensity is inversely proportional to the cross-sectional area of the ray bundle, but  $\psi$  is field amplitude which is proportional to the square root of field intensity.) Consequently, the first level of approximation (equation (34)) by the method of steepest descent represents the field as ordinary plane wave reflection with an appropriate displacement on reflection and geometrical spreading. If the reflection coefficient is considered to be a constant, then there will be no field displacement and equation (34) reduces to the simple plane wave result,

$$\psi = V(\gamma_0) \frac{e^{i[\gamma_0 r + \beta(z+d) - \omega t]}}{\sqrt{r^2 + (z+d)^2}}$$

So far in this section, we have established the relationship between the full wave solution for reflection and the ray theory solution (geometrical spreading) with plane wave reflection. The general criterion for validity of the latter technique is that the quantity  $kR$  be much greater than unity. Another way of considering this criterion is to define a local wavelength angle  $\theta_1$ . At the range in question (the range to the reflector, for example), this is the angle subtended by an arc one wavelength long along the spherical wavefront. Thus,

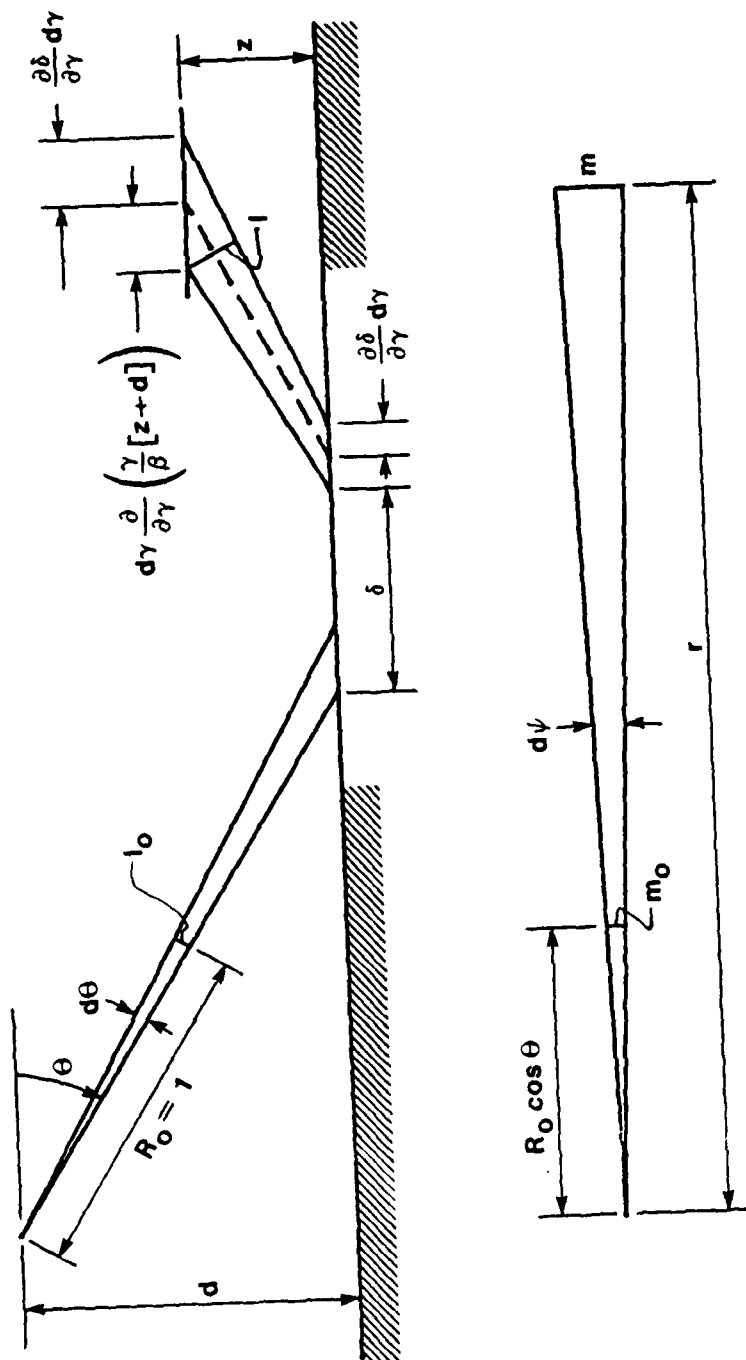


Figure 6. Geometric construction for ray spreading loss including field displacement.



$$kR \gg 1$$

becomes,

$$\theta_\lambda \ll 2\pi$$

where

$$\theta_Y \equiv \frac{\lambda}{R}.$$

Therefore, the validity of the plane wave assumption depends not on the wave-front curvature alone but on the curvature-wavelength product. If one wavelength of arc along the incident spherical wave represents at least a substantial part of a whole circle, then spherical wave theory should be considered.

As we have noted, this is an area in which some caution must be exercised. While we have examined the full solution and an intermediate approximation in which the more pronounced effects of a nonplanar incident wavefront are considered, we must not forget the underlying assumptions. For example, we are depending on slow variation of the magnitude of the reflection coefficient. We are also neglecting the magnitude variation of the  $\sqrt{\gamma/\beta}$  factor in the integrand. Both of these assumptions are violated in certain regions (such as near a critical angle) and we must allow for these violations. In the next section, we will consider an example in which we can see the effects of some of these problem regions and also how to extract meaningful solutions in spite of the difficulties.

#### REFLECTION FROM A THIN LAYER

To illustrate the effects of poles and a branch line integral while maintaining some simplicity in mathematics, let us consider reflection from a finite fluid layer over a rigid reflector as pictured in figure 7. The plane wave reflection coefficient for this case (evaluated at  $z=0$ ) is,

$$V = \frac{\beta_0 \cos \beta_1 h + i b \beta_1 \sin \beta_1 h}{\beta_0 \cos \beta_1 h - i b \beta_1 \sin \beta_1 h} \quad (35)$$

where

$$b = \rho_0 / \rho_1$$

$$\beta_{0,1} = \sqrt{(\omega^2 / c_{0,1}^2) - \gamma^2}.$$

For real angles of incidence ( $\gamma < \omega / c_0$ ), the reflection coefficient magnitude is always one since all the incident energy is returned either by total reflection at  $z=0$  or by reflection from the rigid surface at  $z=-h$ . The reflected field is given by equations (27 and (35). Since equation (35) is symmetric in  $\beta_1$ , but not in  $\beta_0$ , there will only be one branch line integral and that will be

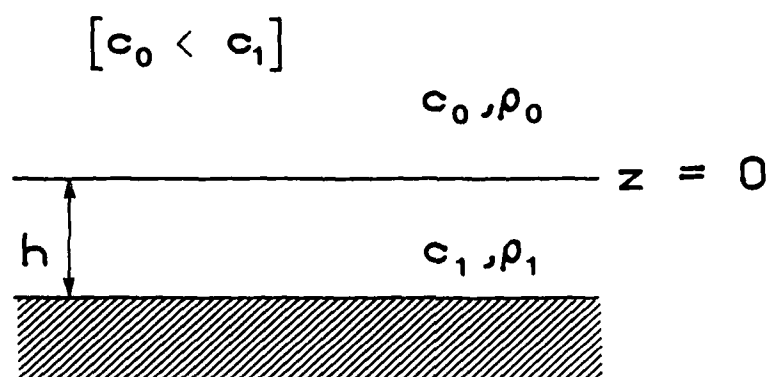


Figure 7. Homogeneous fluid layer over a perfectly rigid reflector.

associated with the pole at  $\beta_0=0$ . In addition, we can expect a number of poles for complex values of  $\gamma$  that are associated with modes partially trapped in the finite layer. Since  $c_1 > c_0$ , there will be no completely trapped modes.

Before we examine the wave theory solution, let us consider what ray theory would predict. There should be one path directly from the source to the upper surface of the layer and back to the receiver. Also, there will be an infinite number of paths that reflect from both the rigid reflector and from the underside of the layer's upper surface some number of times before exiting the layer. These paths will be progressively less important as the number of internal bounces increases since some energy is lost at each reflection with the upper surface of the layer. While we should expect some differences in the wave theory treatment, we would not expect the descent method to predict only a single path, reflected and displaced.

As a starting point for any of the wave solutions, figure 8 shows two possible configurations of the integrand of equation (27) in the complex wave number ( $\gamma$ ) plane. In the first case, deformation of the original integration contour leads to a branch line integral only, while in the second case, residues from each of the poles must be added to a somewhat simpler branch line integral. These techniques are straightforward; however, we must specify the particular branch of  $\beta_0$ . In each of the regions (of the right half-plane) of figure 8, the branches of  $\beta_0$  are as follows,

$$\begin{aligned} \text{I)} \quad \beta_0 &= -\sqrt{k_0^2 - \gamma^2} \\ \text{II)} \quad \beta_0 &= +\sqrt{k_0^2 - \gamma^2} \\ \text{III)} \quad \beta_0 &= +\sqrt{k_0^2 - \gamma^2} \end{aligned}$$

For convenience in the following discussion, we will refer to the sheet of the integrand on which the positive root of  $\beta_0$  is used as the upper sheet and the sheet on which the negative root is used as the lower sheet. By this definition, the poles shown in figure 8 are on the upper sheet. Also, this definition implies a branch cut extending along the real  $\gamma$ -axis to the right of the pole at  $\beta_0=0$ . This is the conventional branch used by computer complex square root routines.

We will now consider a solution by means of the method of steepest descent. Although the numbers are themselves unimportant, we will use the following case to illustrate the method:

$$\begin{aligned} c_0 &= 1500 \text{ m/s} \\ c_1 &= 2000 \text{ m/s} \\ h &= 100 \text{ m} \\ z = d &= 50 \text{ m} \\ \rho_1/\rho_2 &= 0.5 \\ f &= 50 \text{ Hz.} \end{aligned}$$

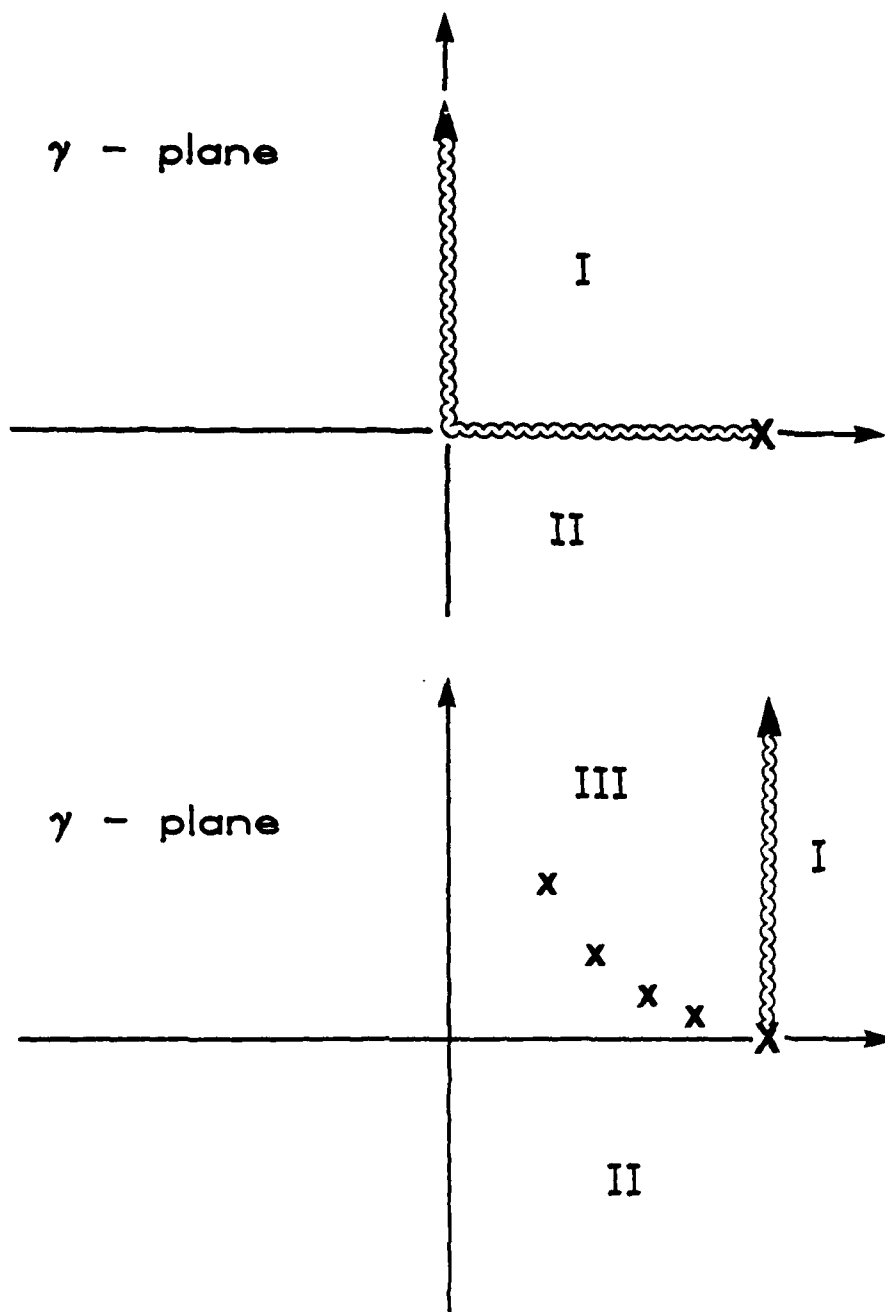


Figure 8. Two possible branch cuts in the  $\gamma$ -plane.

The first step involves locating the saddle points or stationary phase points by means of equation (31). Since the right-hand-side of this equation is independent of the source-receiver geometry, we can plot this function separately and then plot the left-hand-side parametrically in range. The points of intersection determine the stationary phase points. Such a plot is shown in figure 9. Most of the time, each pole (evidenced by the peaks in the field displacement curve) gives rise to a pair of stationary phase points and then there is one additional stationary point to the right of all of the pole pairs. Thus, the influence of each pole (the partially-trapped modes) is felt through a pair of saddle points and the path related to the reflection from the top of the layer is accounted for by the remaining stationary point.

Once the stationary phase points have been located, the contours of steepest descent must be found. In case it is necessary to cross poles or branch cuts in order to deform the original contour into the descent path, the appropriate residues or BLIs must be added to the saddle point solutions. The descent paths for our example (and  $r=300$  m) are shown in figure 10 for only the reflection coefficient and exponential factors of equation (27). The branch cut of figure 8b is used because the descent contour must be continuous. We can see that in the process of deforming the original contour (the real  $\gamma$ -axis) into the descent path, no poles are crossed and the branch cut is avoided. Hence, the solution is complete with only the saddle points considered. Also, notice the path of descent: between each pair of saddle points associated with a pole, the path dips into a zero rather than going to negative infinity. As can be seen from figure 9, as the range increases the two stationary phase points of a pair draw closer together. Consequently, the descent from either saddle into the zero becomes less steep and more terms may be necessary in the approximate solution. Fortunately, the modes which cause this trouble first are the modes that correspond to steeper angles of penetration into and out of the layer and, therefore, lose more energy than the "shallower" modes.

As we have mentioned, the assumption that the  $\sqrt{\gamma/B}$  factor is slowly varying is not always a good assumption. Figure 11 shows the descent paths and saddle points for the entire integrand of equation (27). While the pattern is very similar to that in figure 10, there are some important differences. First, the saddle points have moved slightly (both figures 10 and 11 are exaggerated in the vertical direction by a factor of ten). Since the  $\sqrt{\gamma/B}$  factor could be expressed as a complex exponential, the resulting exponent will add another term to the stationary phase point relation, equation (31), which would predict the shift. Second, as a consequence of the saddle point shift associated with the most lossy mode (farthest to the left and away from the real axis), the descent path has made a definite change. The path passes through only one of the saddle points now and does not venture into the zero below this pole.

From the stationary phase plot in figure 9, we would expect that as the range increases, first, there would be two saddle points for a given mode, then at some particular range, they would somehow coalesce into a single saddle which would then disappear for greater ranges. This is not, in fact, the case as we see in the sequence in figure 12. Here, we have plotted the contours of the entire integrand for three ranges - 200, 300, and 400 m - in the vicinity of the left-most pole-zero combination. At 200 m, the two saddles are nearly symmetrical and the descent path passes through both saddles and the zero. At 300 m, the  $\sqrt{\gamma/B}$  factor has warped the contours so that, because the saddles have drawn closer together, the steepest descent path swings positively upward

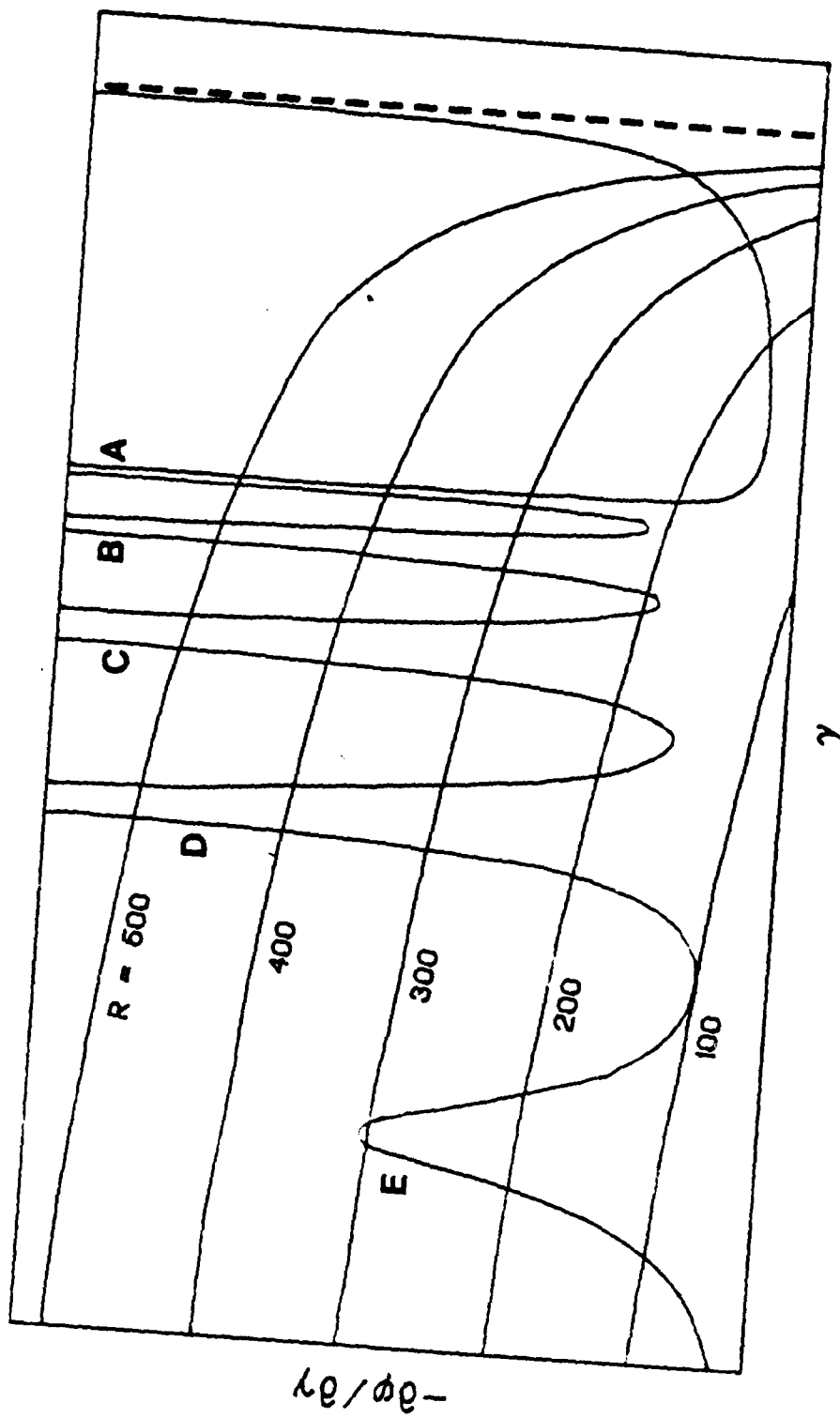


Figure 9. Locator diagram for stationary phase points. Field displacement  $(-\partial\phi/\partial\gamma)$  is plotted as a function of  $\gamma$  and the effects of 5 poles (A - E) are seen.

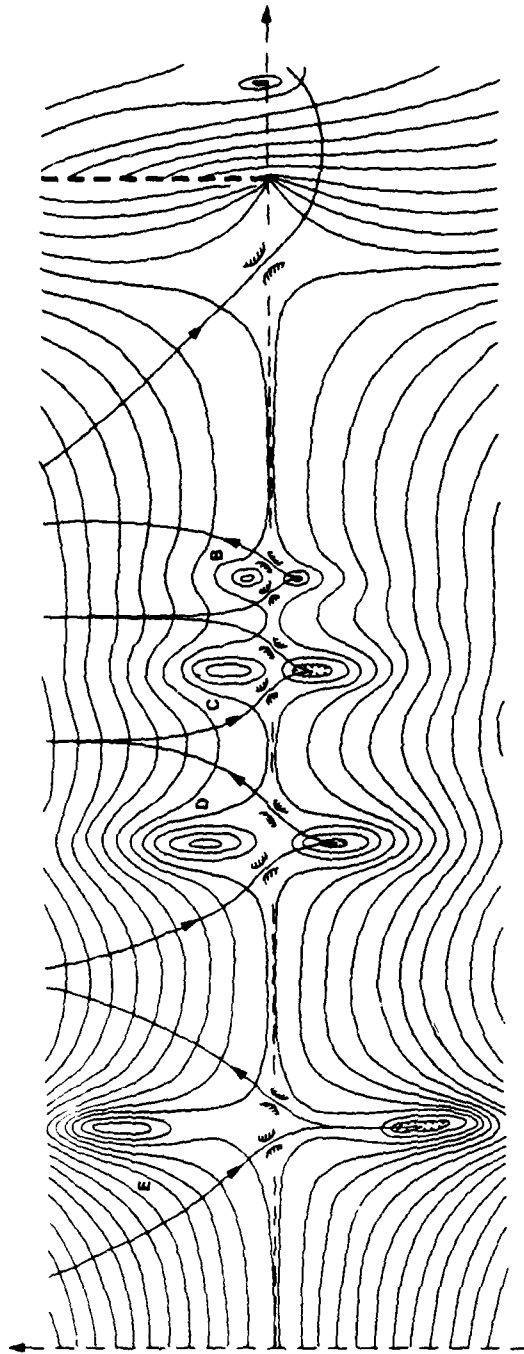


Figure 10. Steepest descent path and saddle points for reflection coefficient and exponential factor of equation (27). Influence of pole A has been omitted to avoid crowding the figure.

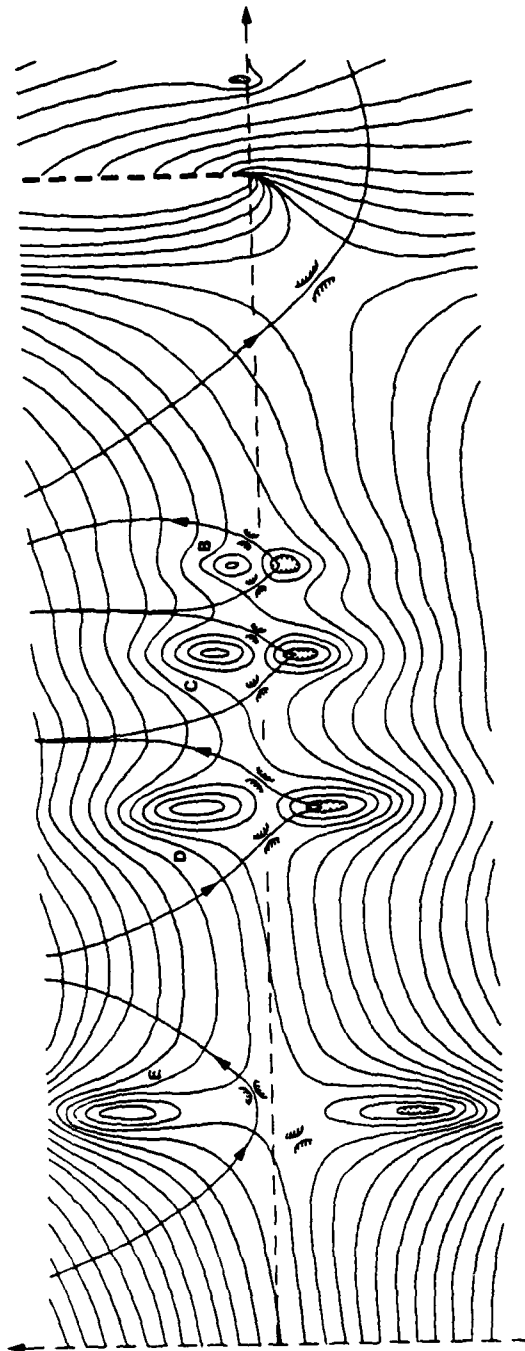


Figure 11. Steepest descent path and saddle points for entire integrand of equation (27).  
As in figure 10, branch cut is shown by vertical dashed line on the right.



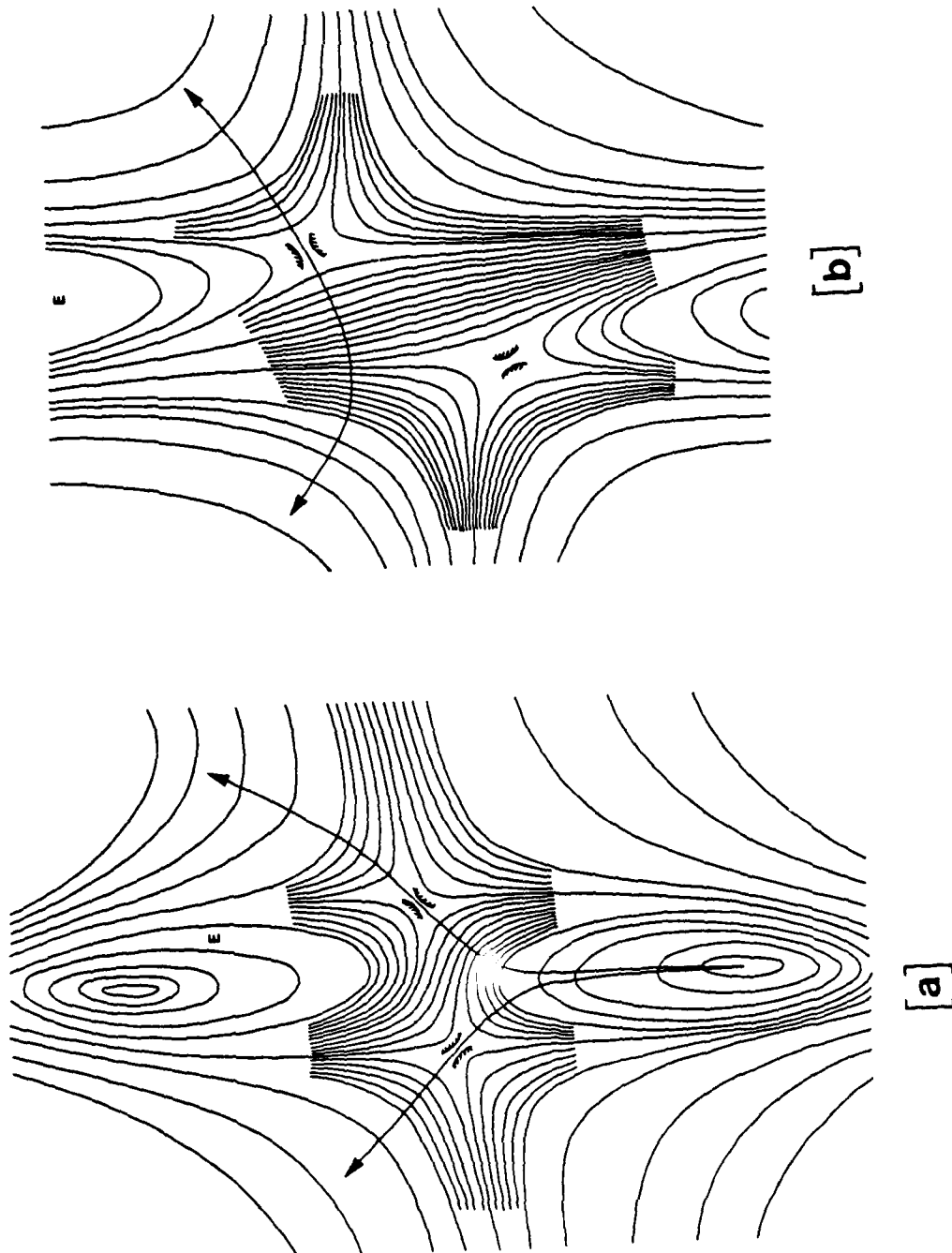
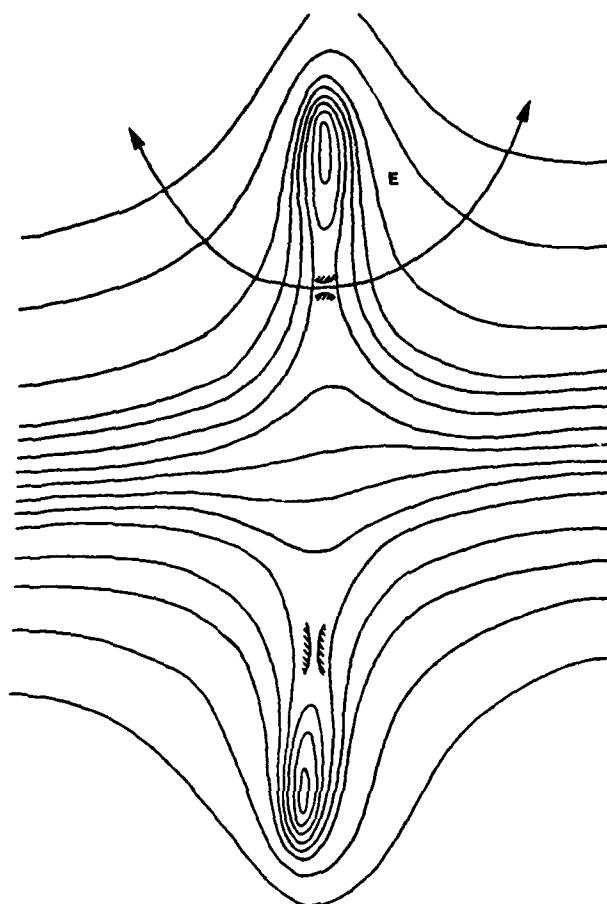


Figure 12. Migration of saddle points and descent contour associated with pole E for increasing range: (a)  $r = 200\text{m}$ , (b)  $r = 300\text{m}$ , (c)  $r = 400\text{m}$ .



[c]

Figure 12. Migration of saddle points and descent contour associated with pole E for increasing range: (a)  $r = 200\text{m}$ , (b)  $r = 300\text{m}$ , (c)  $r = 400\text{m}$  (Continued).

in either direction away from the right-hand saddle. Thus, the left-hand saddle is bypassed in the contour deformation. As the range increases further, the right-hand saddle turns so that the path becomes horizontal while the left-hand saddle turns toward the vertical. The contour plot at  $r = 400m$  illustrates this state and shows that, even though no stationary phase point is predicted by equation (31) through figure 8, one does, in fact, exist with a related descent path. This illustrates a short-coming in equation (31). The steepest descent method will produce the correct answers only if the relevant saddle points are properly identified. Equation (31) gives good approximations for most of these saddle points but, in some instances, one or two may be represented improperly or missed entirely.

Perhaps it is safer practice to solve for the field by a hybrid technique in which we deform the contour past all of the poles but still let it pass through the right-most saddle point in order to avoid the branch line. In this way, the solution becomes a sum of residues and a series approximation at one saddle point.

This solution process tells us something about the resultant signal's phase. Since this modeling effort was undertaken to develop a tool useful for nonlinear signal processing,<sup>1</sup> we are particularly interested in the phase of the field. From figure 9, we can see that the phase change is rapid in the vicinity of the poles of the reflection coefficient. This will lead to problems in phase reconstruction of sampled signals unless the direction of the phase change is known. In order to have a positive field displacement (negative displacements have not been observed in any of the test cases), the rate of change of phase with respect to wave number must be negative by equation (32). Since horizontal wave number is directly proportional to frequency at constant ray geometry, the rate of change of phase with respect to frequency must also be negative:

$$\frac{\partial \phi}{\partial \omega} = \frac{1}{c_v} \frac{\partial \phi}{\partial \gamma}$$

where

$c_v$  = ray equivalent vertex velocity.

If the field displacement is always positive in real physical reflection problems, then we know that the phase progression must be characterized by rapid decreases in the vicinity of the reflection coefficient poles. This principle would be of great value in phase reconstruction of noisy, sampled signals. See reference 1 for a more complete discussion of phase reconstruction problems and techniques.

To summarize this section, let us review the levels of approximation we now have available:

1. By neglecting the rate of phase change of the reflection coefficient, we locate a single stationary phase point which corresponds to specular reflection with no displacement. Any multipath phenomena associated with the reflector are ignored.

2. If we locate all of the stationary phase points (saddle points) that result from considering the reflection coefficient phase variation, then we can write approximations for the multiple paths of propagation from the reflector. The possibility does exist for misinterpreting one or more of these points because of the effects of other factors in the integrand.
3. We can also consider the entire integrand in order to fix the location of the saddle points and descent path. This will improve the accuracy of the saddle point approximations at the expense of substantially increased computational labor.
4. In some cases, the poles themselves may be relatively straightforward to locate, in which case many of the saddle point approximations can be replaced by residues.
5. Finally, the integral can be numerically integrated as it appears in equation (27). This procedure can be expensive particularly when the impulse response of the reflector is desired since an additional integration over frequency is required.

#### NUMERICAL IMPLEMENTATION

Because most of the procedures discussed above are, in practice, applied numerically rather than analytically, we will now consider some numerical techniques for solving the field integral. In order to start with as close to an exact solution as possible, an algorithm has been developed based on Bucker's technique<sup>8</sup> to integrate the field integral, equation (27) directly.

Since variations in the integrand are irregular in that along some portions of the contour the function is smooth and along other portions the function changes rapidly, the integration procedure should be adaptive. This is accomplished by integrating over a segment (in this case, by Gauss-Legendre Quadrature with  $n=5$ ) and comparing this result with the sum of two integrations over the two halves of the same segment. If the difference is negligible, the step size is increased for the next segment. Otherwise, the step size is halved and the integrations are performed again. In this way, the step size is continually adjusted according to the rate of variation of the integrand.

As in some of the processes to follow, a small amount of attenuation is introduced so as to effectively move the integration contour slightly off the real axis. This avoids the complications associated with integration through the pole at  $\beta_0=0$ . The attenuation is treated as viscous attenuation (constant loss per cycle) by adding a small imaginary part to the wave number. Actually, this is done by making the sound speed complex in such a way as to prescribe the appropriate wave number.

Besides direct integration of equation (27), another solution technique involves applying the FFT algorithm to the Fourier transform integral of equation (28). This approach is particularly convenient if we would like the field at many different ranges.<sup>9</sup> Direct numerical integration only gives one range value per integration while, for example, a 512 point FFT would produce field values at 512 evenly spaced ranges. The principal disadvantage of this

method is that the integrand (or, rather, the  $F(\gamma)$  function of equation (28)) varies quite rapidly over some values of  $\gamma$  thereby requiring, as a consequence of the sampling theorems, fine sampling of the entire function. Much of this computational work is wasted because the function can be smooth over other, large segments of  $\gamma$  where the sampling does not need to be as frequent. Since the sampling must be uniform over the entire range of  $\gamma$  (a restriction imposed by the FFT), the regions of rapid variation determine the overall sampling rate and, therefore, the transform size. Without any special treatment then, this method can involve expensive computation of many more points than are necessary to define the function and very large transform sizes.

It is possible, however, to use digital filter theory to greatly increase the efficiency of the FFT technique. Let us consider the development of such a process. Equation (28) can be written in a slightly different form so that the integrand function  $F$  and the field function  $\phi$  are a Fourier transform pair,

$$\phi(r) = \int_{-\infty}^{\infty} F(\gamma) e^{i\gamma r} d\gamma \quad (36)$$

Here, the function  $F$  can be determined from equation (27).

Since  $\phi$  and  $F$  are a Fourier transform pair, we can filter either function in either the wave number or the range domain and also we can expect that once the functions are sampled, the theorem, relating sampling rate and bandwidth, will apply. We shall see later that this is true. Meanwhile, it is sufficient to say that if we can restrict the "bandwidth" of  $\phi$  in the range domain (that is, restrict the span of relevant ranges), then we can sample the function  $F$  at a much lower rate than would normally be required to properly define the function. If we knew  $\phi$ , we could restrict its bandwidth by setting all values of  $\phi$  above some maximum range  $R$  to zero. This is equivalent to filtering  $F(\gamma)$  in such a way that the high rate variations are suppressed (low pass filtering). To perform this operation, then, we must locally sample  $F(\gamma)$  densely enough to describe the function variations, filter these sections, and reduce the sampling rate according to the sampling relations derived below. We then would have an efficient technique for field integral solution by FFT.

Now let us examine the conversion of equation (36) into a discrete Fourier transform suitable for the FFT algorithm. We know that the FFT operates on a finite length series of samples of a function. Since a periodic function can be exactly represented by a Fourier series expansion in place of a continuous Fourier transform, we can convert the integral of equation (36) into a summation if we are willing to accept a field function periodic in range. If we select a period  $R$  that is greater than the maximum range of interest this will not present a problem in itself. We will have to filter  $F(\gamma)$  as discussed above so that  $\phi(r)$  is zero for  $r > R$  prior to sampling  $F(\gamma)$ . If we do not filter, then  $\phi(r)$  will be distorted by aliasing.

To make the summation finite, we can taper  $F(\gamma)$  to zero beyond some maximum  $\gamma$ . This will cause smoothing of the function  $\phi$  (i.e., low pass filtering) in range but this is actually desirable in a wave theory solution. At this point, we have reduced equation (36) to the following form,

$$\phi(k\Delta r) = \sum_{n=0}^{N-1} F(n\Delta\gamma) e^{-ik_n\Delta r\Delta\gamma} \Delta\gamma \quad (37)$$

where

$k, n$  = integer indexes

$\Delta r$  = sample interval of range

$\Delta\gamma$  = sample interval of wave number

$N$  = transform size such that  $N\Delta r = R$ .

One more modification is now necessary before the FFT can be applied. Let,

$$k_n\Delta r\Delta\gamma = 2\pi kn/N$$

or

$$\Delta r\Delta\gamma = 2\pi/N \quad (38)$$

so that,

$$\begin{aligned} \phi(k\Delta r) &= \Delta\gamma \sum_{n=0}^{N-1} F(n\Delta\gamma) e^{-i2\pi kn/N} \\ &= \Delta\gamma \text{FFT} [F(n\Delta\gamma)] \end{aligned} \quad (39)$$

Equation (38) is essentially a statement of the sampling restrictions for this problem. Since we can determine the maximum range  $R$  and

$$R = N\Delta r$$

then the increment  $\Delta\gamma$  is no longer arbitrary but, by equation (38),

$$\Delta\gamma = 2\pi/R \quad (40)$$

and therefore, the relevant span of wave number is,

$$\Gamma = N\Delta\gamma = 2\pi/\Delta r \quad (41)$$

In practice, we would select the transform size and either  $R$  or  $\Delta r$ . This fixes the rest of the parameters and also means that only as many  $F(\gamma)$  points are needed as range points are desired. Once again, the function  $F(\gamma)$  must be initially sampled in such a way that its variations are locally well defined - close sampling in regions of rapid variation and infrequent sampling in regions of slow variation - but then the function is filtered and resampled uniformly and at a low rate given by equation (40). The simplest filter to use is a convolutional filter designed by the window method based on a function in the range domain that is unity between  $r=0$  and  $r=R$  and zero otherwise. The transform of this range function is truncated by one of the standard windows in the wave number domain and then applied in a point-by-point convolution to the  $F(\gamma)$  function. The convolution is only performed at those locations that will be new sample points of  $F(\gamma)$ .

We have seen how the FFT can be used to compute many range points of the field function efficiently. Since this study is primarily concerned with time-domain results, we will now examine the use of the FFT in obtaining time series waveforms from the field integral solutions. Before we considered any of the field integral solutions, we reduced the wave equation to a Helmholtz equation by assuming a time dependence of  $e^{-i\omega t}$ . This reduction could also have been done by taking the Fourier transform of equation (1). We can thus see that, in order to obtain the time series, we need only take the inverse Fourier transform of the field function  $\phi$ . Hence,

$$p(t) = \frac{1}{2\pi} \int_{-\infty}^{\infty} \phi(\omega) e^{-i\omega t} d\omega \quad (42)$$

where

$p$  = pressure as a function of time.

This is basically the same result as equation (18). Notice that the independent variable in the function  $p$  is frequency  $\omega$  rather than range. As a result, we must compute the field function at many frequencies and a single range for each  $p(t)$  function.

As before, we can recast equation (42) in a form suitable for using the FFT.

$$\begin{aligned} p(n\Delta t) &= \Delta f \sum_{k=0}^{N-1} p(k\Delta f) e^{-i2\pi kn/N} \\ &= \Delta f \text{FFT}^{-1} [:(k\Delta f)] \end{aligned} \quad (43)$$

where

$\Delta f$  = discrete form of  $d\omega/2\pi$

$N = 1/(\Delta t \Delta f)$ .

The pressure response  $p$  is the impulse response whose spectrum is given by  $\phi(\omega)$ . The implied impulse strength can be found by evaluating equation (43) at  $n = 0$  (which is to say  $t=0$ ),

$$p_0 = N \Delta f$$

or

$$p_0 \Delta t = N \Delta f \Delta t = 1$$

which is the impulse strength. We will find it convenient to make all of the time-domain (impulse response) calculations in terms of impulse strength so that the results are independent of transform size. We will then compute,

$$p(n\Delta t)\Delta t = \frac{1}{N} \text{FFT}^{-1}[\phi(k\Delta f)] \quad (44)$$

Before we leave our discussion of numerical techniques, let us consider two more aspects of the FFT techniques. One of these we have mentioned before and that is the inclusion of the source waveform by spectrum multiplication. In particular, we will be modeling a source in the next section that can be approximated by an exponential function,

$$s(t) = Ae^{-\alpha t} \quad (t > 0)$$

where

$\alpha$  = decay time constant.

First, we would like to normalize the source so that, when applied by convolution to a uniform level, it does not change the power of the time function. This can be assured by letting,

$$1 = \int_0^{\infty} Ae^{-\alpha t} dt$$

or

$$A = \alpha$$

Therefore, we will use a normalized source function of,

$$s(t) = \alpha e^{-\alpha t} \quad (t > 0) \quad (45)$$



although it will be applied by multiplying the field function  $\phi(\omega)$ , by the source spectrum  $S(\omega)$ ,

$$S(\omega) = \int_0^{\infty} \alpha e^{-\alpha t} e^{i\omega t} dt$$

$$= \alpha \left[ \frac{\alpha + i\omega}{\alpha^2 + \omega^2} \right] \quad (46)$$

and the desired pressure response is then,

$$r(t)\Delta t = \frac{\alpha}{N} \text{FFT}^{-1} \left[ \left[ \frac{\alpha + i\omega}{\alpha^2 + \omega^2} \right] \phi(\omega) \right]$$

where

$r$  = simulated received signal.

Finally, the truncation of  $\phi(\omega)$  beyond some maximum frequency introduces spurious oscillations into the  $p(t)$  function. The truncation is necessary because of the finite length of the transform; however, the truncation does not have to be abrupt. If we taper the upper edge of the  $\phi$  spectrum by some function (perhaps half a cycle of a raised cosine) prior to transforming, we can reduce these oscillations substantially. In practice then, the simulated received signal is computed as follows,

$$r(t)\Delta t = \frac{\alpha}{N} \text{FFT}^{-1} \left[ \left[ \frac{\alpha + i\omega}{\alpha^2 + \omega^2} \right] W(\omega)\phi(\omega) \right] \quad (47)$$

where

$W(\omega)$  = weighting function.

## APPLICATIONS

One of the first decisions that must be made in using these models for transient propagation is whether to use a model based on plane waves or spherical waves. Predictions based on plane wave theory are generally fast and easily applied to complicated multipath propagation. On the other hand, there are instances in which the plane wave assumptions lead to grossly incomplete results. In this section, we will discuss those effects predicted by both the plane and spherical wave theories, develop the criteria for decision between the two, and illustrate prediction by the full wave theory.

Generally, the plane wave theory is used as an adjunct to ray or geometrical acoustics. Spreading losses and refraction in the water are accounted for by ray tracing and the ray path is modified in magnitude and phase at the ocean floor according to the plane wave reflection coefficient. We will add to this the possibility of a displacement (or even multiple displacements) on reflection from the ocean floor because this phenomenon is included by the degenerate form of the full solution, equation (34). This displacement is a legitimate feature of the field as long as the magnitude of the reflection coefficient is slowly varying with wave number.

Plane wave theory then includes the following effects: time delay, refraction, and spreading in the water by ray acoustics; phase and magnitude changes and field displacement on reflection from the ocean floor; and phase distortion at ray turning points. The last effect amounts to a uniform  $\pi/2$  phase shift at a turning point (caused by refraction) and is evidenced by formation of doublets in the time series (a single positive impulse becomes a positive impulse followed immediately by a negative impulse). This doublet formation is obvious in the time series and can be used to identify refraction turning points either in the water column or in the ocean floor. Most of the other effects are more difficult to use in direct interpretation of measurement signals but the time delay is valuable for isolating distinctly different propagation paths.

Figure 4 illustrates the construction of a plane wave model that treats a number of different paths. Each path is characterized by a water path delay and loss, and a bottom reflection characterized by the plane wave reflection coefficient. Since the paths are not mutually dependent, they can be added or deleted as necessary to represent any aspect of an ocean environment. This feature, coupled with the dependence of the reflection coefficient only on angle, yields a model that can be easily adapted to different situations. This approach should be used whenever it is applicable because it is not only flexible but also very inexpensive compared to the spherical wave solution.

As we will outline more specifically, there are important applications in which the plane wave solution is inadequate. Besides the effects covered by the plane wave model, the spherical wave solution includes boundary waves of several types and ducted propagation in layered or refracting bottoms. Particularly at low frequency or in shallow water, these mechanisms can contribute a substantial, if not dominant, portions of the received energy.

In the case in which the ocean floor is modeled as a homogeneous fluid, an interface wave can be excited which travels horizontally while continuously radiating energy back into the overlying ocean. This interface wave is excited by energy incident to the boundary at the critical angle and the re-radiation appears to be coming from the boundary at that same critical angle. Because of the continuous re-radiation associated with this boundary wave, the energy in the advancing wave decays much more rapidly than the specularly reflected wave. (The amplitude of the interface wave drops at approximately  $r^{-2}$  while that of the reflected wave drops at  $r^{-1}$ .) As a result, this interface wave is only significant at shorter ranges, but it can change the propagation characteristics substantially at ranges where the specular reflection is close to the critical angle (figure 13). This type of wave is also known as a critically refracted wave or lateral wave.

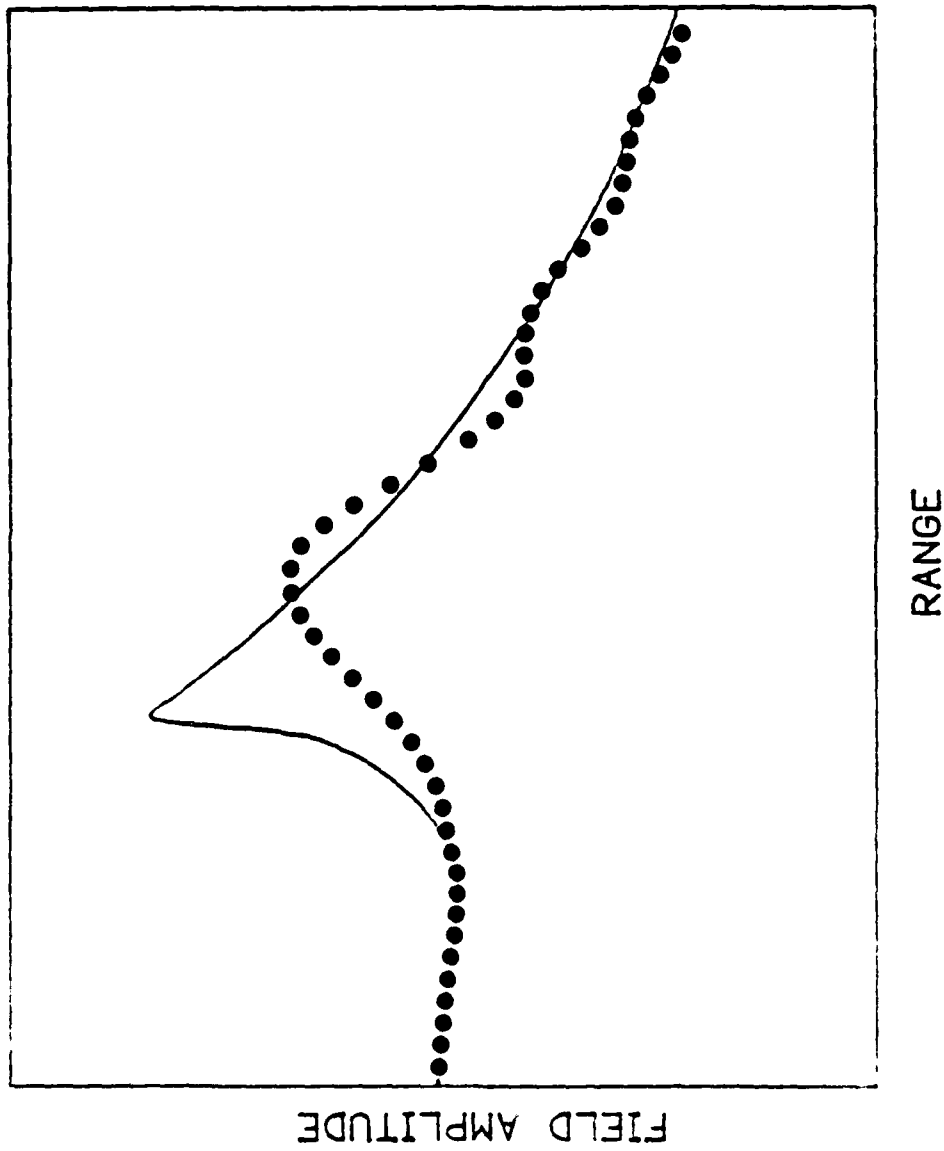


Figure 13. Comparison of ray/plane-wave solution (—) with spherical wave solution (....) near critical angle reflection from fluid half-space

If the fluid representing the ocean floor is layered or has a sound speed profile that produces a duct, then partially trapped or ducted propagation can take place. Ray theory can be used to model ducting but, especially when the acoustic wavelength is of the order of the duct width, the integral wave theory provides much better representation of the ducted energy. Typically, there will be a number of stationary phase points corresponding to the poles which, in turn, represent the leaky modes in the duct.

Additional types of waves appear if the bottom model is made of an elastic material (that is, a solid). At least two other types of interface waves can propagate in this case: a shear wave analogous to the compressional interface wave for the fluid reflector and a Stoneley wave in which the particle motion is confined to the vertical plane containing the source and receiver. The Stoneley wave has its own pole in the reflection coefficient for some complex wave number and it loses energy (as does the other shear interface wave) at a rate similar to that of the compressional interface wave.

Ducts caused by solid layers or gradients in the shear sound speed give rise to ducted shear propagation or Love waves. One notable characteristic of either shear or compressional ducted propagation is that it is dispersive: different frequencies travel with different speeds. This results in a distortion of the time waveshape that the plane wave technique is unable to describe. This also can make replica deconvolution (inverse filtering) difficult since the dispersion effectively distorts the source waveform.

An important aspect of shear propagation in real ocean sediments is attenuation. Shear attenuation is generally much greater than compressional attenuation because sediments are much closer to fluids than solids even though they do have some rigidity. Consequently, if solid properties are accounted for by the model, attenuation must be included. Otherwise, the shear propagation can be unrealistically good.

Having summarized the scope of both the plane wave and the spherical wave solutions, let us now outline the criteria for deciding which to use. As we have shown, the mathematical criteria for validity of the plane wave approximation are  $kr \gg 1$  (so that the asymptotic form of the Hankel function can be used) and  $kR \gg 1$ . These are roughly equivalent and the latter criterion amounts to insuring that a wavelength is small compared to the wavefront circumference at the radius of interest. Another way of saying this is that  $2\pi$  times the wavefront's radius of curvature must be much greater than the acoustic wavelength.

If we desire to simplify the plane wave theory even further by neglecting field displacement and multiple stationary points, we need some additional restrictions. First, trapped propagation in the bottom must be negligible. Trapped modes are evidenced by poles in the reflection coefficient and these poles will either lead to multiple stationary phase points or residues. Second, the geometry must be such that the critically refracted or Stonely interface waves are not favorably excited. In order to avoid exciting the critically refracted wave, the geometry must be such that the ordinary reflected path (source to interface to receiver) is not very close to the critical angle. If this path is close to critical, then the reflection coefficient magnitude is changing rapidly and plane wave theory, even with displacement, is not valid.

Whether or not the Stoneley wave is favorably excited is not as easy to determine. The Stoneley wave pole of the reflection coefficient must be found and then the wave number corresponding to that pole must be used in equation (31) to establish the critical geometry. Since we only need the geometry approximately, it should be acceptable to ignore the displacement term (the right-hand-side) of equation (31) and, also, to use the real part of the wave number rather than the true saddle point value.

To conclude this section, let us examine several examples of the full wave solution and compare these results to actual measurements. The measurements, made by Roever and Vining,<sup>10</sup> are high-quality scale model measurements of short pulse reflection from several substances with both compressional and elastic properties.

Some objections may be raised at this point because these measurements are scale-model measurements and not actual ocean measurements. In spite of the vast quantity of ocean acoustic measurements available at various Navy and university laboratories, measurements that are well-defined in terms of precise experimental geometry, physical parameters of the medium, and characteristics of the source and also are well documented as to experimental procedures are rare. Initial validation of a model against the usual types of measurements would involve considerable "adjustment" of the physical parameters in order to get good agreement. This technique, although common, always includes the possibility that the medium properties were adjusted not to correct deficiencies in their initial estimates but to offset problems in the model itself. I preferred, in this investigation, to use a data set that I could model without such manipulations.

In each of the three cases, the experiment consisted of a spark-gap source and a barium titanate receiver fixed 10 cm apart and 0.5 cm above the reflecting material in salted tap water. The frequency content of the source pulse and the medium properties and experimental geometry were such that the horizontal range was between 10 and  $0.1 \lambda$  ( $\lambda$  is acoustic wavelength). This presents the most difficult modeling problem possible as wavefront curvature is definitely important and, at the same time, the asymptotic methods are not valid. Hence, the modeling in this section was done by integration of the field integral, equation (25), and subsequent integration over frequency by FFT using equation (47).

Physical parameters for the water and reflecting media were measured by Roever and Vining and included compressional and shear sound speed, compressional and shear attenuation, and density. Since these properties were measured on the same scale as the experiment itself, the property estimates were used, as given in reference (10), with no modifications.

The first material considered was a high viscosity pitch with the following acoustic properties:

Water over Pitch

$$c_1 = 1496 \text{ m/sec}, c_2 = 2463 \text{ m/sec}$$

$$b = 1003 \text{ m/sec}, \rho_2/\rho_1 = 1.27$$

$$A_c = 1 \text{ dB/cm at } 500 \text{ kHz}$$

$$A_s = 0.6 \text{ dB/cm at } 25 \text{ kHz}$$

where

$$c_1 = \text{sound speed in water}$$

$$c_2 = \text{compressional speed in lower medium}$$

$$b = \text{shear speed in lower medium}$$

$$\rho_1 = \text{density in water}$$

$$\rho_2 = \text{density in lower medium}$$

$$A_c = \text{compressional attenuation in lower medium}$$

$$A_s = \text{shear attenuation in lower medium.}$$

The measured and the predicted time waveforms at the receiver are plotted in figure 14.

Overall, the agreement between the predicted signal and the actual measurement is excellent. The first feature, arriving at about 50  $\mu\text{sec}$  after transmission, is the compressional interface wave. Next, just prior to 70  $\mu\text{sec}$ , the direct and simply-reflected arrivals appear but they are not individually distinguishable because the travel time difference between the two paths is only about 1/8  $\mu\text{sec}$ . Finally, the Stoneley wave arrives between 100 and 150  $\mu\text{sec}$ . Since the shear sound speed in the pitch is less than the sound speed in the water, there is no critically refracted shear wave in this case.

This example is of particular practical importance because ocean sediments are usually only weakly elastic with low shear speed and high shear attenuation. These factors might lead to a conclusion that the shear propagation could be neglected, but there is a considerable amount of energy in the Stoneley wave in this example. As long as the reflector has some shear rigidity, there will be a Stoneley wave pole in the reflection coefficient. In this case, that pole corresponds to a phase velocity of 821 m/sec which is considerably lower than the shear speed of the pitch. Hence, the Stoneley wave arrives last.

One very important consideration when modeling shear propagation in sediments is the inclusion of shear attenuation. Since the Stoneley wave can be a fairly efficient transporter of energy at short ranges, if attenuation is neglected, the Stoneley wave can appear to dominate the arrival. The water-over-pitch example was run with zero shear attenuation and, while the events before 100  $\mu\text{sec}$  remained virtually unchanged, the Stoneley wave arrival grew both in its positive and negative cycles to the point where the negative peak (at about 130  $\mu\text{sec}$ ) was more than three times the amplitude of the direct arrival peak at 68  $\mu\text{sec}$ . Obviously, this would have resulted in a gross over-estimate of the role of shear propagation. As it is in figure 14, the level of the predicted Stoneley wave is slightly less than the actual event. This difference is not surprising considering the difficulty of measuring shear attenuation.

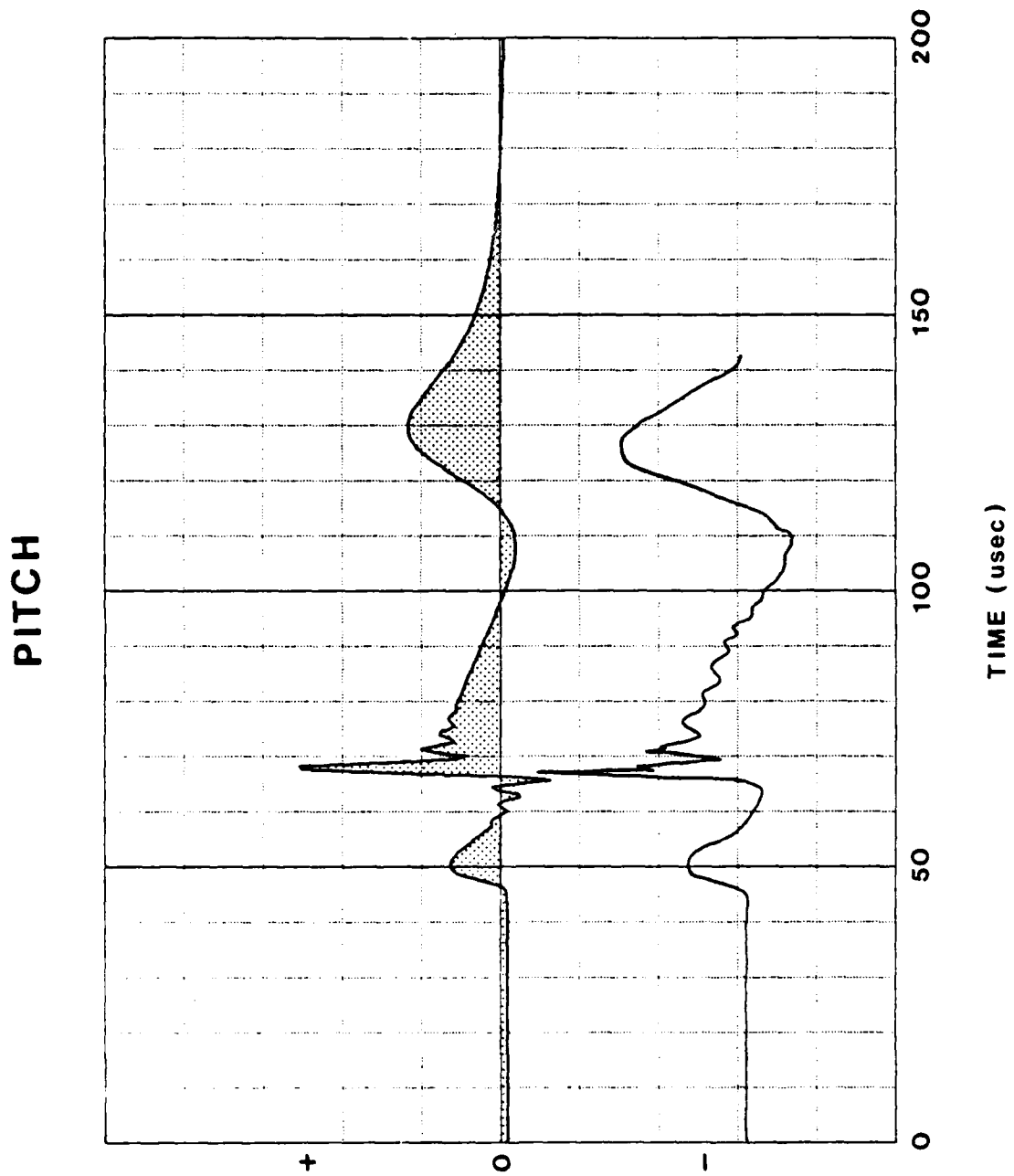


Figure 14. Predicted time series for reflection from pitch by spherical wave theory. Measurement is displaced below predicted curve.

The next reflecting medium was cured plaster-of-paris and the experimentally determined properties were:

Water over Plaster

$$c_1 = 1484 \text{ m/sec}, c_2 = 3192 \text{ m/sec}$$

$$b = 1814 \text{ m/sec}, \rho_2/\rho_1 = 1.89$$

$$A_c = 0.6 \text{ dB/cm at } 500 \text{ kHz}$$

$$A_s = 0.2 \text{ dB/cm at } 25 \text{ kHz.}$$

The three features present with pitch can be seen here again in figure 15. The compressional interface wave is much lower in level (the vertical scale is identical to that of figure 14) appearing at 40  $\mu\text{sec}$ . At about 70  $\mu\text{sec}$ , the combined direct/reflected pulse appears and a rather large amplitude Stoneley wave appears between 60 and 100  $\mu\text{sec}$ . The direct arrival is at about the same place as before because the water has almost the same sound speed in both cases, but both the compressional interface wave and the Stoneley wave have arrived earlier because the speeds in plaster are higher than those in pitch. Also, the plaster is more rigid with less attenuation of shear waves so the Stoneley wave amplitude is larger.

An additional event can be seen at 60  $\mu\text{sec}$  and this, according to Strick,<sup>10</sup> is a combination of a small, critically refracted shear wave and a psuedo-Rayleigh wave. Both of these waves are interface waves that travel at the shear speed of the lower medium.

Finally, the results for water over iron are shown in figure 16 and the physical properties are tabulated below,

Water over Iron

$$c_1 = 1500 \text{ m/sec}, c_2 = 5837 \text{ m/sec}$$

$$b = 3247 \text{ m/sec}, \rho_2/\rho_1 = 7.87$$

$$A_c = 0.01 \text{ dB/cm at } 500 \text{ kHz}$$

$$A_s = 0.01 \text{ dB/cm at } 25 \text{ kHz.}$$

No attenuation measurements were made in this case by Roeber and Vining so very small values were used merely to avoid numerical problems associated with integration exactly along the real axis.

Because the impedance discontinuity is extremely large in this case (the compressional impedance ratio is over 30), the combination direct/reflected arrival dominates the waveform. The Stoneley wave is much shorter in time than before and only the negative cycle can be seen at about 66  $\mu\text{sec}$ . A very small compressional interface component is just visible at 25  $\mu\text{sec}$  and, again, there is a combination shear interface and pseudo-Rayleigh wave at 40  $\mu\text{sec}$ . As in the other two examples, the agreement between the theory and the experiment is excellent.



# PLASTER OF PARIS

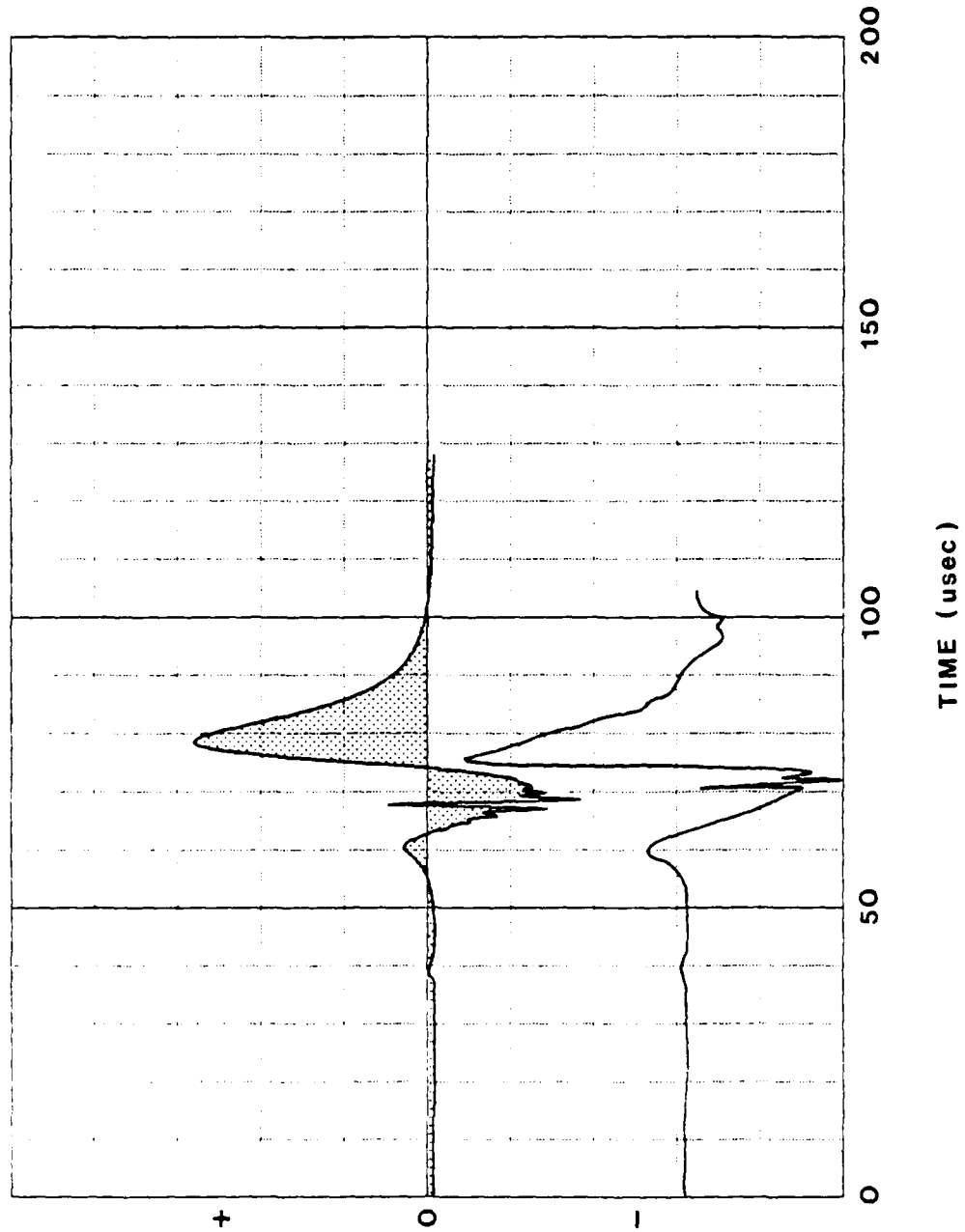


Figure 15. Predicted time series for reflection from plaster-of-paris. Measured waveform is lower curve.

# IRON

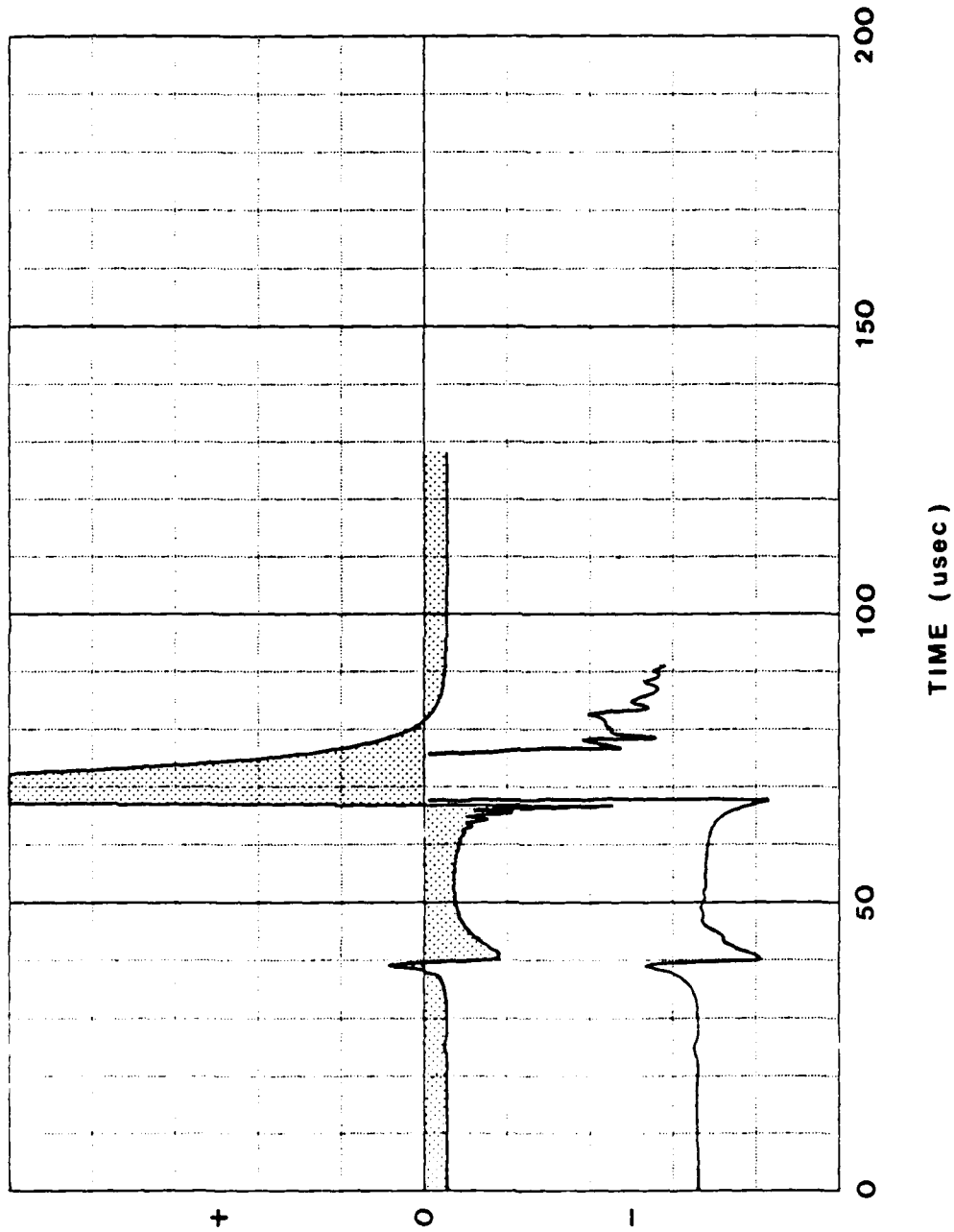


Figure 16. Predicted time series for reflection from iron. Lower curve is measurement.

These examples are, in one sense, difficult problems because the wave effects are fully developed so that even the asymptotic methods do not work well. They are, however, simple examples in that the reflector is a homogeneous half-space. More complicated reflector structures can easily be accommodated though, since the model really only needs a reflection coefficient and, given enough time, this can be computed for very complicated structures (see appendix A).

## CONCLUSIONS

In this work, we have examined two general types of models for propagation of transient acoustic signals. For one type, we developed the field integral that exactly represents the acoustic field for a given source and medium. The other type is actually a very special case of the exact solution. If enough assumptions are valid, the field can also be represented by ray theory with plane wave reflection at boundaries. The latter model is much simpler and more flexible; however, these advantages are gained by sacrificing some important features of propagation associated with wavefront curvature. In many cases, wavefront curvature is negligible but, when it is not, some form of the field integral must be evaluated.

Whatever model is used must suit the environment in question. In deep water or at high frequency, the plane wave model may be quite accurate. At low frequency, near the ocean floor or in or near leaky ducts, the plane wave model may omit significant or dominant propagation mechanisms.

Fortunately, there are some techniques that are intermediate in complexity and still offer at least approximations to the full wave solutions. The saddle point or steepest descent method reduces the field integral to one or more integrals that can be evaluated over short intervals and, possibly, some residues or branch line integrals. As long as the true saddle points are located and all of the poles and branch lines are accounted for, this approach is still exact. The first approximation that can be made is to integrate only over a small region near each saddle point. Also, we can neglect the offset of the saddle points from the real axis. At this point, the procedure can be coupled with ray theory for each of the possible paths and some representation of interface waves, trapped modes, and field displacement will be maintained. Finally, if the phase of the reflection coefficient is neglected, the solution reduces to classical ray theory with a single specular reflection at the ocean floor.

The decision to use either plane wave or spherical wave methods should be based on the wavefront curvature criterion. If an acoustic wavelength is an appreciable part of the circumference of the acoustic wave at the boundary, then the full wave solution is justified. Some weight must be given to the relative cost of the approaches though. The ray theory model is easily adapted to complex multipath situations and is fast and inexpensive to run. In some cases, this may justify its use even when the full wave solution is indicated by the wavefront curvature criterion, as long as the shortcomings of the ray approach are acknowledged.

We have seen both in the theoretical development and in the experimental comparisons that the models can be used to interpret propagation results physically. The plane wave and ray theory approach obviously treats each path distinctly. The saddle point method also breaks the solution down into a number of physically distinct "paths" and special wave effects may be interpreted in light of these components.

Finally, we have outlined several ways in which the FFT can be used to speed the calculations required by these models. The integration over frequency can be done very easily using the FFT and, at the same time, the source spectrum can be included so that the resulting response is not the impulse response but, instead, a simulation of the complete received response. In addition, the field integration over wave number is suited to evaluation by FFT, especially if results are required at many different source-to-receiver ranges.

REFERENCES

1. Gabrielson, T.B., "Impulse response of the ocean floor: nonlinear techniques for measurement enhancement," NADC-82253-30, 1982.
2. Rubisch, J.R. and Haas, P.S., "A summary of NAVAIRDEVCEEN ocean acoustic bottom loss measurements (U)," NADC-80169-30 (C), 23 July 1981.
3. Brekhovskikh, L.M., Waves in Layered Media, Academic Press, NY, 1960.
4. Bucker, H.P., "Sound propagation in a channel with lossy boundaries," J. Acoust. Soc. Am. 48, pp. 1187-1194, 1970.
5. Stratton, J.A. Electromagnetic Theory, McGraw-Hill, NY, 1941.
6. Abramowitz, M. and Stegun, I., Handbook of Mathematical Functions, Dover, NY, 1972.
7. Gabrielson, T.B., "Mathematical foundations for normal mode modelling in waveguides," NADC-81284-30, 1981.
8. Bucker, H.P. "Propagation in a liquid layer lying over a liquid half-space (Pekeris cut)," J. Acoust. Soc. Am. 65, No. 4, pp. 906-908, 1979.
9. DiNapoli, F. and Davenport, R., "Theoretical and numerical Green's function field solution in a plane multilayered medium," J. Acoust. Soc. Am. 67, No. 1, pp. 92-105, 1980.
10. Roever, W.L.; Vining, T.F. and Strick, E., "Propagation of elastic wave motion from an impulsive source along a fluid/solid interface," Phil. Trans. Roy. Soc. London A251, pp. 455-523, 1959.
11. Erdelyi, A., Asymptotic Expansions, Dover, NY, 1956.
12. Bartberger, C.L. and Ackler, L., "Normal mode solutions and computer programs for underwater sound propagation," NADC-72001-AE, 4 April 1973.

Appendix A  
REFLECTION FROM MULTILAYERED MEDIUM

Appendix A  
REFLECTION FROM MULTILAYERED MEDIUM

In order to provide for future expansion of the reflection model, the plane wave reflection coefficient for a general, multi-layered medium is derived below. Although this derivation could just as easily be done for any quantity that satisfies the wave equation, we will write expressions in terms of velocity potential.

The generalized medium is shown in figure A-1. In each layer or in the fluid half-space above the layers, the expression for the field is,

$$\phi_i = a_i p_i(z) + b_i q_i(z) \quad (z_{i-1} \leq z \leq z_i) \quad (A-1)$$

where

$a_i, b_i$  = constants

$p_i, q_i$  = independent solutions of the depth equation

$\phi_i$  = velocity potential in  $i^{\text{th}}$  layer

The equation for  $\phi_0$ , the potential in the fluid half-space, can be written more specifically in terms of the overall reflection coefficient  $V_t$ ,

$$\begin{aligned} \phi_0 &= \text{const} \left[ e^{-i\beta_0 z} + V_t e^{i\beta_0 z} \right] \\ &= a_0 e^{-i\beta_0 z} + b_0 e^{i\beta_0 z} \end{aligned}$$

therefore,

$$V_t = \frac{b_0}{a_0} = \frac{1}{r_0} \quad (A-2)$$

where

$$r_i = a_i / b_i.$$

The boundary conditions between each pair of layers are,

(1) continuity of pressure

$$\phi_i(z_i) = \phi_{i+1}(z_{i+1})$$

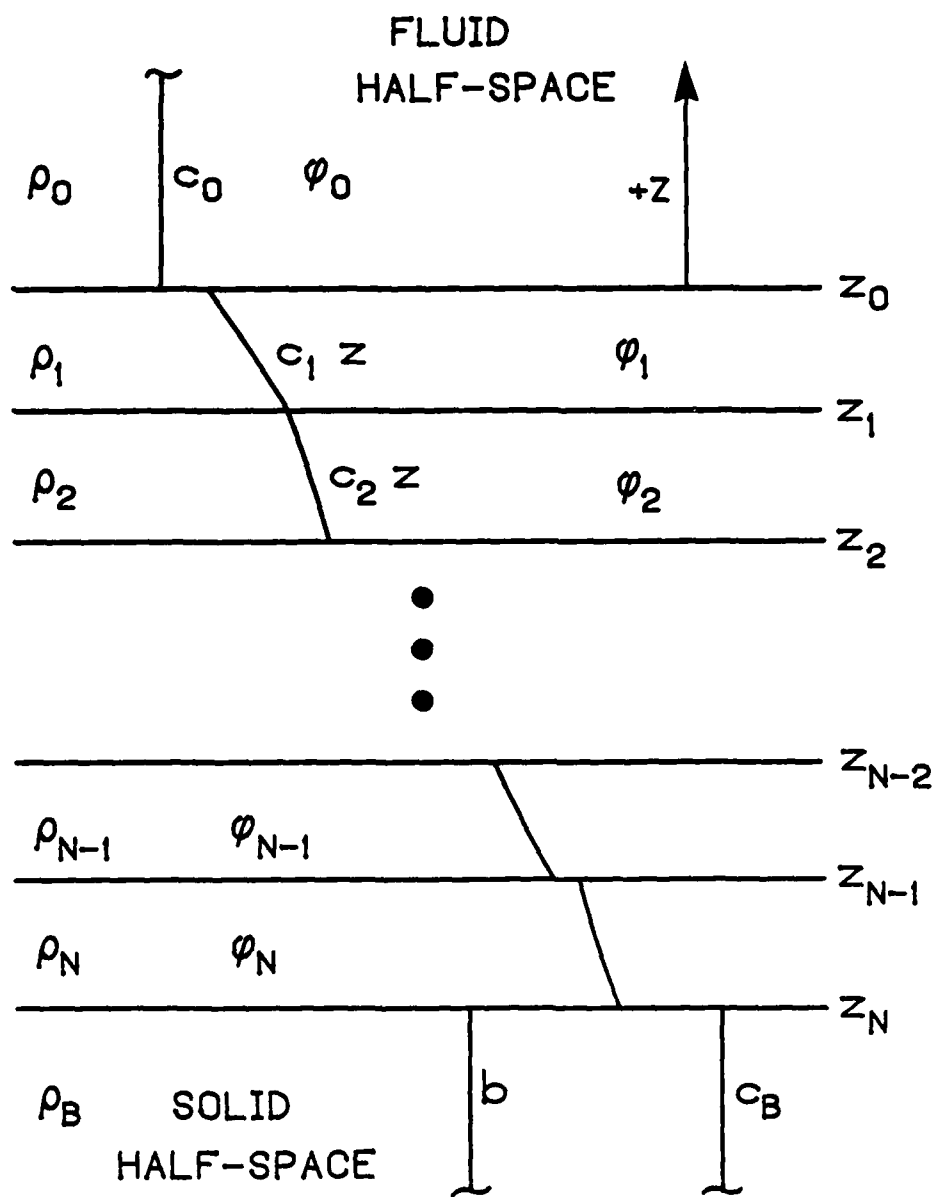


Figure A-1. Generalized model of the ocean floor as a layered reflector.



(2) continuity of normal component of velocity

$$\left. \frac{\partial \phi_i}{\partial z} \right|_{z_i} = \left. \frac{\partial \phi_{i+1}}{\partial z} \right|_{z_i}$$

These two equations can be written as one expression relating the ratio of coefficient in the  $i$ th layer to the ratio of coefficients in the layer below,

$$r_i = \frac{-q_i [r_{i+1} p'_{i+1} + q'_{i+1}] + q'_i [r_{i+1} p_{i+1} + q_{i+1}] \rho_{i+1} / \rho_i}{p_i [r_{i+1} p'_{i+1} + q'_{i+1}] - p'_i [r_{i+1} p_{i+1} + q_{i+1}] \rho_{i+1} / \rho_i} \quad (A-3)$$

where the  $p$  and  $q$  function are evaluated at  $z=z_i$  and the primes indicate differentiation with respect to  $z$ .

The solution process generally begins at the solid basement half-space and proceeds upwards layer by layer until  $r_0$  and, therefore,  $V_t$  are found. Equation (A-3) relates any two adjacent layers and equation (A-2) yields the total reflection coefficient  $V_t$ . In order to start the process at the fluid-solid interface at  $z_N$ , we use the impedance condition, equation (5), and solve for the initial coefficient ratio  $r_N$ ,

$$r_N = \frac{-q_N(z_N) + \xi q'_N(z_N)}{p_N(z_N) - \xi p'_N(z_N)} \quad (A-4)$$

where the bottom impedance involves the elastic half-space reflection coefficient from equation (4).

If the sound speed in the layered bottom becomes considerably greater than the phase velocity of the incident wavefront (that is, the vertex velocity of the equivalent ray), then it is neither necessary nor desirable to start at the elastic half-space. As the medium sound speed increases beyond the phase velocity, the depth function decays in an approximately exponential manner. Starting the solution all the way down at the elastic half-space would mean starting with an extremely small field amplitude. Any error in the original value would grow unacceptably large by the time the top of the reflecting layers was reached.

This problem is avoided by including a false basement of homogeneous fluid at some depth where the local sound speed is substantially greater than the phase velocity. If the sound speed of the false bottom is matched to the real profile at this point, the equivalent impedance is,

$$\xi = i/\Delta_f$$

where

$$\beta_f = \sqrt{k^2(z_f) - \gamma^2}$$

$z_f$  = depth of false bottom.

This impedance value is inserted into equation (A-4) and the solution progresses from  $z_f$  to the reflector surface at  $z=0$  in the usual way.

Appendix B  
AIRY FUNCTIONS

## Appendix B AIRY FUNCTIONS

### Origin of Airy Functions

Airy functions arise as special solutions of the depth equation that results from separation of variables of the wave equation. This wave equation, in axially-symmetric cylindrical coordinates,

$$\frac{1}{r} \frac{\partial}{\partial r} \left( r \frac{\partial \psi}{\partial r} \right) + \frac{\partial^2 \psi}{\partial z^2} = \frac{1}{c^2} \frac{\partial^2 \psi}{\partial t^2}$$

where

$c$  = sound speed

$r$  = horizontal range

$t$  = time

$z$  = depth

$\psi$  = field quantity (pressure, for example),

reduces to a Helmholtz equation for harmonic disturbances and then separates into a range equation involving Bessel functions and a depth equation,

$$\frac{d^2 U}{dz^2} + [k^2(z) - \gamma^2] U = 0 \quad (B-1)$$

where

$k = \omega/c(z)$

$U$  = depth function

$\gamma$  = horizontal wave number from range equation

$\omega$  = angular frequency ( $2\pi f$ ).

If the sound speed  $c$  is constant, the solutions of equation (B-1) are sines and cosines; however, we would like to be able to specify some variation in sound speed with depth. Since the  $z$ -variation of equation (B-1) is of the form  $1/c^2$ , we can make the equation linear in  $z$  if we let,

$$\frac{1}{c^2(z)} = \frac{1}{c_0^2} - g(z - z_0) \quad (B-2)$$

where

$c_0$  = sound speed at  $z = z_0$

$g = \left( \frac{1}{c_1^2} - \frac{1}{c_2^2} \right) / (z_2 - z_1)$  = pseudo-gradient.

thus, equation (B-1) can be written as,

$$\frac{d^2 U}{dz^2} + \left[ \left( \frac{\omega^2}{c_0^2} - \gamma^2 \right) - g\omega^2(z - z_0) \right] U = 0. \quad (B-3)$$

Being linear in  $z$ , this equation can be simplified by the following transformation,

$$Z = a \left[ \left( \frac{\omega^2}{c_0^2} - \gamma^2 \right) - g\omega^2(z - z_0) \right]$$

$$\frac{dZ}{dz} = -ag\omega^2$$

Equation (B-3) then becomes,

$$a^2(g\omega^2)^2 \frac{d^2 U}{dZ^2} + \frac{1}{a} ZU = 0$$

which is Stoke's equation,

$$\frac{d^2 U}{dZ^2} - ZU = 0 \quad (B-4)$$

if

$$a = -(g\omega^2)^{-2/3}$$

or

$$Z = q(z - z_0) - \frac{1}{q^2} \left( \frac{\omega^2}{c_0^2} - \gamma^2 \right) \quad (B-5)$$

where

$$q = (g\omega^2)^{1/3}$$

Stoke's equation is second order; therefore, it has two linearly independent solutions. A particular set of these solutions comprises Airy functions or, in symbolic notation,  $Ai(Z)$  and  $Bi(Z)$ .

#### Standard Series Forms For Airy Functions<sup>6</sup>

The standard form of the ascending series is a linear combination of the ordinary power series solutions to equation (B-4).

$$Ai(Z) = a_1 f(Z) - a_2 g(Z) \quad (B-6)$$

$$Bi(Z) = \sqrt{3} [a_1 f(Z) + a_2 g(Z)]$$

where

$$a_1 = \text{Ai}(0)$$

$$a_2 = \text{Ai}'(0)$$

$$f(Z) = 1 + \frac{1}{3!} Z^3 + \frac{1 \cdot 4}{6!} Z^6 + \frac{1 \cdot 4 \cdot 7}{9!} Z^9 + \dots$$

(B-7)

$$g(Z) = Z + \frac{1}{4!} Z^4 + \frac{2 \cdot 5}{7!} Z^7 + \frac{2 \cdot 5 \cdot 8}{10!} Z^{10} + \dots$$

These series are valid for any complex  $Z$  although as the magnitude of  $Z$  increases, the number of terms required for a given accuracy also increases. For this reason, various other series representations have been derived.

Asymptotic series, as they are called, are series that are valid when the argument approaches some limiting value (infinity in this case). They are not necessarily convergent series and the best accuracy is obtained by summing until the terms start to increase in magnitude. For the Airy functions, these asymptotic series are derived by applying the method of steepest descent to the Airy integrals<sup>11</sup>. The derivation procedure is unimportant for this discussion so we will merely list the various forms and their ranges of applicability<sup>6</sup>:

Definitions -

$$c_0 = 1, c_k = \frac{(2k+1)(2k+3)\dots(2k+4k-1)}{216^k k!}$$

(B-8)

$$d_0 = 1, d_k = -\frac{6k+1}{6k-1} c_k$$

$$\zeta = \frac{2}{3} Z^{3/2}$$

(B-9)

$$S_a = \sum_{k=0}^{\infty} (-1)^k c_k \zeta^{-k}, \quad S_b = \sum_{k=0}^{\infty} (-1)^k d_k \zeta^{-k}$$

$$S_e = \sum_{k=0}^{\infty} (-1)^k c_{2k} \zeta^{-2k}, \quad S_{ep} = \sum_{k=0}^{\infty} (-1)^k d_{2k} \zeta^{-2k}$$

$$S_o = \sum_{k=0}^{\infty} (-1)^k c_{2k+1} \zeta^{-2k-1}, \quad S_{op} = \sum_{k=0}^{\infty} (-1)^k d_{2k+1} \zeta^{-2k-1}$$

$$\zeta' = \zeta + \frac{\pi}{4}$$

Exponential forms -

$$\begin{aligned} \text{Ai}(Z) &= \frac{1}{2^{1/2}} Z^{-1/2} e^{-Z} S_a & / \arg Z / < \pi \\ \text{Ai}'(Z) &= -\frac{1}{2^{1/2}} Z^{1/2} e^{-Z} S_b & / \arg Z / < \pi \end{aligned} \quad (\text{B-10})$$

$$\begin{aligned} \text{Bi}(Z) &= \frac{1}{2^{1/2}} Z^{-1/2} e^{-Z} S_a & / \arg Z / < \pi/3 \\ \text{Bi}'(Z) &= \frac{1}{2^{1/2}} Z^{1/2} e^{-Z} S_b & / \arg Z / < \pi/3 \end{aligned} \quad (\text{B-11})$$

Oscillatory forms -

$$\text{redefine } \gamma = \frac{2}{3}(-Z)^{3/2}$$

$$\begin{aligned} \text{Ai}(Z) &= \frac{1}{\sqrt{\pi}} (-Z)^{-1/4} [S_e \sin \gamma - S_o \cos \gamma] & / \arg Z / > 2\pi/3 \\ \text{Ai}'(Z) &= -\frac{1}{\sqrt{\pi}} (-Z)^{1/4} [S_{ep} \cos \gamma + S_{op} \sin \gamma] & / \arg Z / > 2\pi/3 \end{aligned} \quad (\text{B-12})$$

$$\begin{aligned} \text{Bi}(Z) &= \frac{1}{\sqrt{\pi}} (-Z)^{-1/4} [S_e \cos \gamma + S_o \sin \gamma] & / \arg Z / > 2\pi/3 \\ \text{Bi}'(Z) &= \frac{1}{\sqrt{\pi}} (-Z)^{1/4} [S_{ep} \sin \gamma - S_{op} \cos \gamma] & / \arg Z / > 2\pi/3 \end{aligned} \quad (\text{B-13})$$

Special oscillatory forms for Bi -

$$\text{redefine } \gamma = \frac{2}{3} (Ze^{\mp i\pi/3})^{3/2}$$

$$\begin{aligned}
 \text{Bi}(Z) &\approx \sqrt{\frac{2}{\pi}} e^{+i\pi/4} Z^{-1/4} \left[ S_e \sin(\zeta' + \frac{i}{2} \ln 2) \right. \\
 &\quad \left. - S_o \cos(\zeta' + \frac{i}{2} \ln 2) \right] \quad /(\arg Z) + \frac{\pi}{3} / < 2\pi/3 \\
 \text{Bi}'(Z) &\approx \sqrt{\frac{2}{\pi}} e^{+i\pi/4} Z^{1/4} \left[ S_{ep} \cos(\zeta' + \frac{i}{2} \ln 2) \right. \\
 &\quad \left. + S_{op} \sin(\zeta' + \frac{i}{2} \ln 2) \right] \quad /(\arg Z) + \frac{\pi}{3} / < 2\pi/3
 \end{aligned} \tag{B-14}$$

As long as the magnitude of  $Z$  is great enough to insure sufficient accuracy of the asymptotic series, one or another of these can be used to compute the Airy functions or their derivatives in any region of the complex  $Z$ -plane.

#### Problems In Numerical Computation

It is evident from equations (B-6) and (B-7) that there is a region on and around the positive real  $Z$ -axis in which the terms of the series for  $\text{Ai}$  (and  $\text{Ai}'$ ) alternate in sign. The individual terms become very large as the series progresses thus requiring the differences of large numbers. Since these differences should be small as the series converges, the numerical range imposed by quantization in the computer word is exceeded very quickly.

Consequently, the ascending series cannot be computed far enough in  $Z$  to match satisfactorily with the asymptotic series of equations (B-10). Even with the 120-bit double precision words of the CDC Cyber 170 computer, only seven decimal digits are correct at the best matching point between the ascending and asymptotic series. The more common 64-bit double precision word would restrict the accuracy even further, perhaps to the point of creating problems in iterative calculations.

#### Origin-Translated Ascending Series

The solution to this problem lies in modifying the ascending series so that the terms do not alternate in sign. This is easily done by solving the differential equation (B-4) with a power series expanded around a point displaced along the positive real  $Z$ -axis. Let,

$$t = Z - Z_0 \tag{B-15}$$

where

$Z_0$  = origin point for the series,

so that equation (B-1) becomes,

$$\frac{d^2 U}{dt^2} - (t + Z_0) U = 0. \tag{B-16}$$



Set up the power series solution in terms of the new variable  $t$ ,

$$U = \sum_{n=0}^{\infty} a_n t^n \quad (B-17)$$

and substitute into equation (B-16). By equating the coefficients of like powers of  $t$ , we can form the following relationships in which  $a_0$  and  $a_1$  are arbitrary,

$$a_2 = \frac{Z_0}{2} a_0 \quad (B-18)$$

$$a_{n+2} = \frac{a_{n+1} + Z_0 a_n}{(n+2)(n+1)}$$

or

$$U(Z) = a_0 + a_1 t + \frac{Z_0}{2!} a_0 t^2 + \frac{1}{3!} [a_0 + Z_0 a_1] t^3 + \dots$$

from which we see that,

$$\begin{aligned} a_0 &= U(Z_0) \\ a_1 &= U'(Z_0) \end{aligned} \quad (B-19)$$

The conditions of equations (B-19) allow us to develop the Airy functions if we know  $Ai(Z_0)$  and  $Ai'(Z_0)$  (or, of course,  $Bi(Z_0)$  and  $Bi'(Z_0)$ ). Notice that  $Z_0$  is not restricted to being real although we will only consider the real case since this will solve our particular accuracy problem.

In the following section, we will consider the problem of finding the starting values  $Ai(Z_0)$  and  $Ai'(Z_0)$  as well as the errors of each of the other series over their regions of validity in the  $Z$ -plane. At this point, it should be mentioned that the origin-shifted series completely eliminates the computational problems involved with the usual ascending series. When the origin-shifted series is evaluated for  $Z$  less than  $Z_0$ , the terms are no longer alternating in sign and the series converges rapidly.

#### Error Analysis

Except for the problem region (roughly a  $+30^\circ$  wedge centered on the positive real  $Z$ -axis) discussed above, the standard against which each of the series was evaluated is a double precision (120-bit word or about 29 decimal digits) ascending series based on equations (B-6). After some experimentation, I selected  $|Z| = 6$  as the crossover point between the single precision ascending series and the asymptotic series. Figure B-1 shows the number of digits that correspond exactly with the double precision ascending series for each form of the single precision series at  $|Z| = 6$ . The problem around the positive real axis can be seen readily in the exponential case and the ascending series case

for  $A_i$  (note the circled numbers). In addition, we can see over what regions the other series should be used if, as in this case, we would like at least eight decimal digits to be correct using only single precision (60-bit).

Since no series shown in figure B-1 covers the  $|\arg Z| < \pi/6$  region adequately, we must now consider the origin-shifted series. The error of an asymptotic series is shown in reference (11) to be of the order of the last term included. This term is easily computed because beyond this point the terms grow. Hence, we must compare successive terms<sup>12</sup>,

$$a_i \zeta^{-i}, \quad a_{i+1} \zeta^{-i-1}$$

until the  $i+1$ th term is larger than the  $i$ th term or,

$$\frac{a_{i+1}}{a_i \zeta} > 1.$$

The coefficients are independent of  $\zeta$ ; therefore, for any  $\zeta$ , this point can be easily calculated. The size of the  $i$ th term then gives the order of accuracy of the summation.

In this work, the exponential asymptotic series gave a satisfactory value at  $Z = 12$ , so I first generated an origin-shifted series about this point. As shown in figure 2, this series tracked well with the asymptotic series down to  $Z = 7$ . Next, I constructed a series with its origin at  $Z = 8$  using the values of  $A_i(8)$  and  $A_i'(8)$  from the  $Z = 12$  series. This new series was evaluated all the way back to  $Z = 0$  and, as seen in figure B-2, the agreement with the double precision zero-origin series is excellent below  $Z = 4$ . This shows that even the double precision (120-bit) ascending series deteriorates rapidly beyond  $Z = 5$ . Finally, the  $Z = 8$  series was used to compute  $A_i(6)$  and  $A_i'(6)$  - the starter values for the series actually used in the Airy function algorithm. These values could have been calculated from the  $Z = 12$  series to roughly the same accuracy but this was not apparent until the  $Z = 8$  series had been tested.

#### Routine For Calculation of Airy Functions

Based on the error study summarized in the last section, the argument plane (the complex  $Z$ -plane) was divided into the regions shown in figure B-3. These regions and the associated forms of the Airy function series are as follows,

- I)  $|Z| < 3$  : ascending series ( $Z_0 = 0$ ) for  $A_i$  and  $B_i$  - equations (B-6),
- II)  $3 \leq |Z| \leq 6$ : ascending series ( $Z_0 = 0$ ) for  $B_i$  - equation (B-6) and
  - a)  $|\arg Z| < \pi/6$ : ascending series ( $Z_0 = 6$ ) for  $A_i$  - equation (B-17),
  - b)  $|\arg Z| > \pi/6$ : ascending series ( $Z_0 = 0$ ) for  $A_i$  - equation (B-6),

- III)  $|Z| \geq 6$ : a)  $|\arg Z| \geq 2\pi/3$ : oscillatory asymptotic series for  $Ai$  and  $Bi$  - equations (B-12) and (B-13),  
 b)  $|\arg Z| < 2\pi/3$ : exponential series for  $Ai$  - equation (B-10) and special oscillatory series for  $Bi$  - equation (B-14).

The starting values for the ascending series are:

I)  $Z_0 = 0$

$$Ai(0) = 0.355\ 028\ 053\ 888$$

$$Ai'(0) = -0.258\ 819\ 403\ 793$$

$$Bi(0) = \sqrt{3}\ Ai(0)$$

$$Bi'(0) = -\sqrt{3}\ Ai'(0)$$

II)  $Z_0 = 6$

$$Ai(6) = 0.994\ 769\ 436\ 025 \times 10^{-5}$$

$$Ai'(6) = -0.247\ 652\ 003\ 970 \times 10^{-4}$$

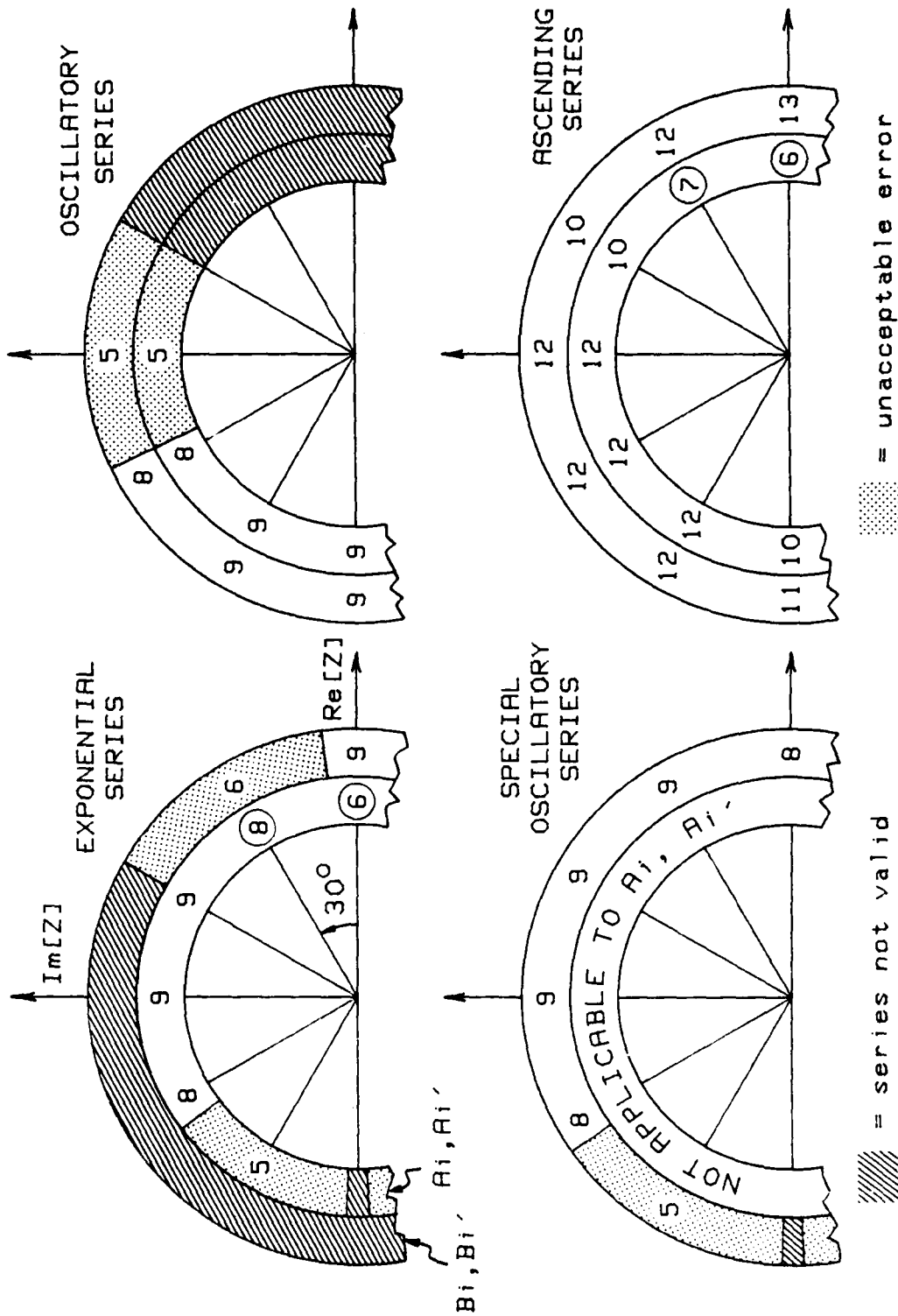
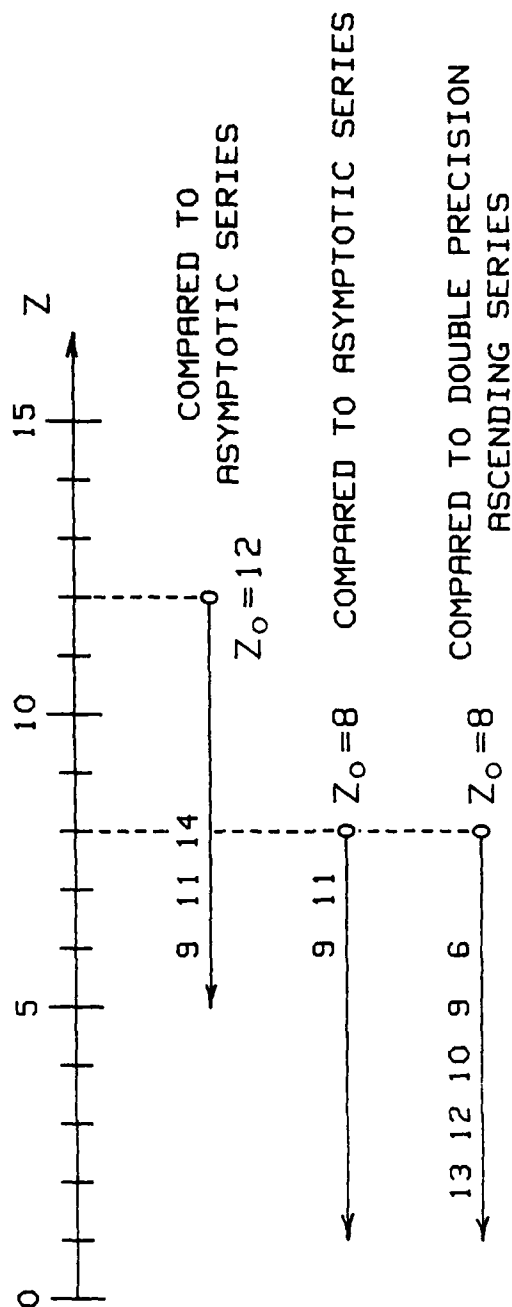


Figure B-1. Correct digit comparison for Airy series.



Performance of single precision origin-shifted series for  $A_i$  and  $A_i'$  along the positive real axis. Numbers shown are numbers of digits that equal those corresponding digits of either the asymptotic series or the double precision ascending series.

Figure B-2. Origin-shifted series analysis.

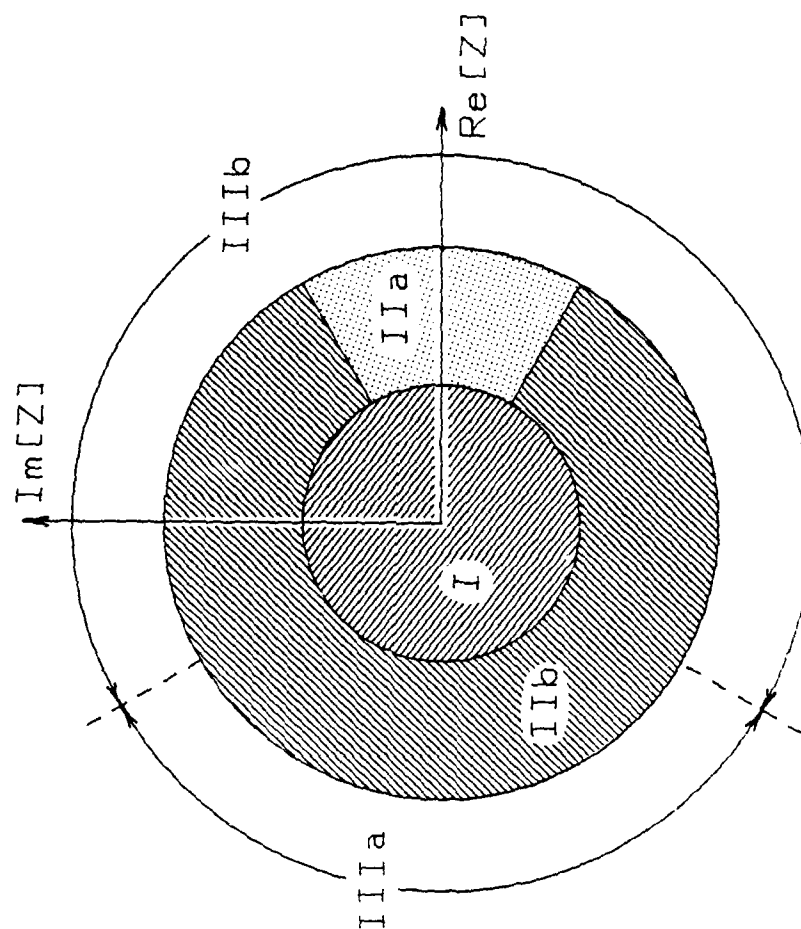


Figure B-3. Division of complex  $Z$ -plane for numerical computation of Airy functions.

# DISTRIBUTION LIST (Cont.)

	<u>No. of Copies</u>
Applied Physics Laboratory The Johns Hopkins University Johns Hopkins Road Laurel, MD 20707	1
Lamont-Doherty Geological Observatory Palisades, NY 10964	1
Woods Hole Oceanographic Institution Woods Hole, MA 02543	1
Scripps Institute of Oceanography Marine Physics Laboratory San Diego, CA 92152	1
Auditory Research Laboratory Northwestern University 2299 Sheridan Road Evanston, IL 60201 (Dr. Frederic Wightman)	1
DTIC	12